From the Klinik für Radiologie und Neuroradiologie
(Director: Prof. Dr. med. Olav Jansen)
at the University Medical Center Schleswig-Holstein, Campus Kiel
at Kiel University

LIGHT SIGNAL ATTENUATION BY MURINE CORTICAL BONE FOR QUANTIFICATION OF FLUORESCENCE REFLECTANCE IMAGING

Dissertation
to acquire the doctoral degree (Dr. med.)
at the Faculty of Medicine
at Kiel University

presented by
LENNART MARTIN BITTERMANN
from **Hamburg**

Kiel **2019**

1^{st} Reviewer:	Prof. Dr. rer. nat. Claus-Christian Glüer, Klinik für Radiologie und Neuroradiologie
2^{nd} Reviewer:	Priv.-Doz. Dr. med. habil. Ulf Lützen, Klinik für Nuklearmedizin, Molekulare Bilddiagnostik und Therapie
Date of oral examination:	08.09.2020
Approved for printing, Kiel,	26.03.2020

Signed: Prof. Dr. med. Johann Roider
(Chairperson of the Examination Committee)

Contents

Abbreviations

BMD Bone mineral density

CCD Charge-coupled device

CI_{95} 95 %-confidence interval

CT Computed tomography

FMT Fluorescence molecular tomography

FRI Fluorescence reflectance imaging

DNA Deoxyribonucleic acid

GFP Green fluorescent protein

LED Light emitting diode

μCT Micro-computed tomography

mfp Mean free path

PBS Phosphate buffered saline

ROI Region of interest

TMD Tissue mineral density

CHAPTER 1

Introduction

1.1 Fluorescence Imaging

Fluorescent dyes are applied as contrast agents in a great number of imaging techniques. These techniques can be found in clinical medicine allowing for example the fast determination of the type and concentration of cells within a patient's blood sample via the fluorescence-based flow cytometry (Bruhn *et al.*, 2011). Fluorescent contrast agents are also routinely applied to monitor retina and choroid vessels in patients suffering from diabetic retinopathy or age-related macular degeneration (Grehn, 2008) to name just another technique in every day clinical diagnostics. But the relevance of fluorescence imaging is even bigger in preclinical research, where this technique is used to investigate the physiology and pathophysiology of cells ranging from fluorescent labelling of cellular and extracellular structures to monitoring the dynamics of gene expression (Sanderson *et al.*, 2014).

1.1.1 Physical Principles of Fluorescence

A major advantage of fluorescent imaging in comparison to other imaging techniques, such as computed tomography or scintigraphy, is the use of non-ionising electromagnetic waves within the visible ($400 - 750\ nm$, Cox (2019)) and near-infrared ($650 - 900\ nm$, Ntziachristos *et al.* (2005)) wavelength spectrum. High energy radiation, such as X-rays, can potentially harm the organism under investigation by damaging macro-molecules within the cell, such as the genetic make-up (DNA, deoxyribonucleic acid) (Kauffmann *et al.*, 2011). But high energy radiation is also a potential harm to the operator executing the research. This is why an experimental set up without ionising radiation is both safer and simpler as cell damage from ionisation can be neglected and radiation protection is not necessary (Graves *et al.*, 2004).

Electromagnetic radiation, such as visible and near-infrared light, can physically be described either as a wave or as a particle. Its wave nature is characterized by electric and magnetic fields oscillating perpendicular to each other and the direction of propagation. It travels at the speed of light ($c \approx 3 \times 10^8\ m/s$) and is further characterized by its wavelength (λ) and oscillation

frequency (f) via the relationship: $c = \lambda f$. But it was found in the early twentieth century that light also exhibits properties which can be better explained considering it as a particle, *the photon*. This definition includes a quantized amount of photon energy (E, where $E = h f$ and h corresponds to *Planck's constant*) that can only be dissipated completely during an interaction with matter, such as a molecule (Cox, 2019).

These interactions can be explained by the molecular orbital theory, which states that the electrons of any given molecule can also only contain discrete (or quantized) levels of energy. Each of these energy levels can be occupied by two electrons with differing *spins*, which is another quantized property of elementary particles similar to angular momentum in classical physics. The two spin states of an electron are either *up* or *down* in quantum mechanics (Vogel, 1999). A promotion of an electron to a certain higher energy state via light interaction is thus only possible, if this energy state is not already occupied and the photon's energy is exactly equal to the energetic difference of the two concerned electronic states. If these conditions are met, the photon is absorbed and the molecule is promoted to a higher electronic (also called an *excited*) state. The lowest energetic state is called the *ground* state. But a molecule can also absorb energy in other ways, such as vibration, this is related to the resonance frequencies of molecular bonds. Common resonance frequencies of carbon-hydrogen-bonds correspond to mid-infrared frequencies of electromagnetic waves, which can thus be used to promote a molecule to a vibrational exited state. As the photons of this radiation contain less energy than the ones of visible light, the energetic differences between ground and excited state are smaller compared to absorption processes involving visible light. The amount of energy which can be dissipated by a molecule is again quantized. Excited states are usually energetically non-favourable states and are therefore instable. They tend to quickly relax back to their intial stable ground state. This is basically a reversed excitation process, in which different kinds of quantized energy are dissipated by the molecule again (Cox, 2019).

The absorption and emission of light by a molecule is generally called *photoluminescence*. More specifically, this process is called *phosphorescence*, if excited states of a given molecule last for up to two seconds before relaxing back into the ground state. In the case of *fluorescence*, the time interval in which the molecule remains in the excited state after the absorption of light is many orders of magnitude smaller (typically 10^{-6} s) (Abramowitz & Davidson, 2019). But a process which occurs even faster is the *non-radiative decay*. It corresponds to the loss of vibrational energy and can be thought of as heat, which is dissipated to the surroundings of a fluorescent molecule. After a molecule is promoted to an excited state, it only takes picoseconds ($= 10^{-12}$ s) for the vibrational excited state to decay. The emission of the fluorescent light always occurs after the molecule has already dissipated a fraction of the absorped energy as vibrational energy, this is why the emitted photon is always of lesser energy and therefore longer wavelength than the one that has been absorbed. This difference between the absorbed and emitted photons is called the *Stokes shift*. The probability with which a photon is absorbed and emitted at a given wavelength by a certain fluorescent molecule can be visualized with absorption and emission spectra presented in figure 1.1 (a). The fact that the absorption and emission spectra are not single lines, but a broad spectrum of wavelengths, is due to the above described vibrational energy states, which allows light with slightly differing wavelengths to still

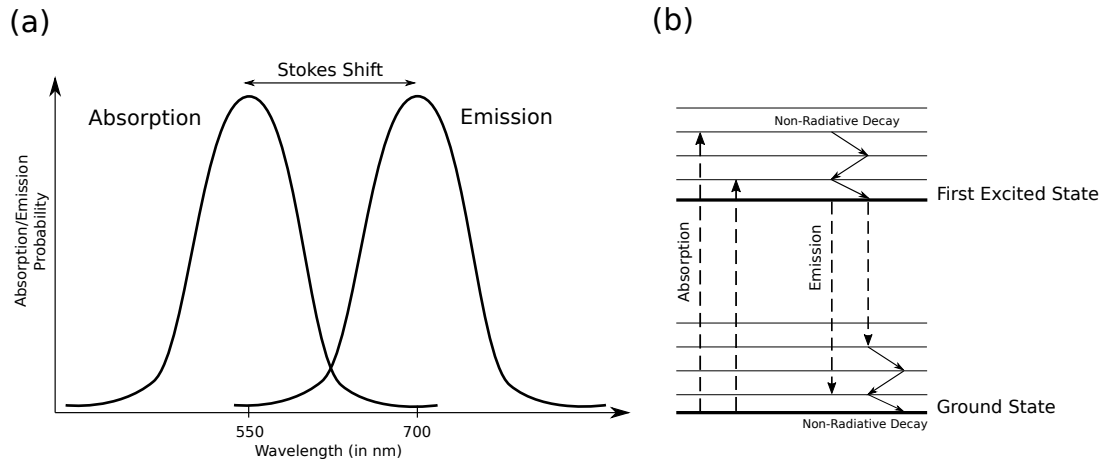

Figure 1.1: **Physical principles of fluorescence.** (a) Typical absorption and emission spectra of a fluorescent dye. (b) Jablonski diagram including examples for energy level changes due to absorption and emission of photons. Adapted from Cox (2019) (graphics program: Inkscape 0.91, opensource vector graphics editor, `http://www.inkscape.org`).

be absorbed, while non-radiative decay may occur not only before, but also after the photon emission. Figure 1.1 (b) shows a simplified diagram of the energy levels of a molecule including examples of electronic energy level changes due to absorption and emission of photons. This so called *Jablonski diagram* summarises the above described physical principles of fluorescence (Cox, 2019).

1.1.2 Fluorescent Proteins

Osamu Shimomura and Frank Johnson were the first to isolate a protein from the *Aequorea victoria* jellyfish in 1961 that would emit green fluorescence after applying ultra-violet light, the *green fluorescent protein* (GFP) (Piston *et al.*, 2019a). The technological progress of the following years then allowed to succesfully sequence the DNA of this protein in the early 1990*s* (Prasher *et al.*, 1991). This allowed the incorporation of the GFP-DNA into host cells (known as transfection, Plattner & Hentschel (2006)), which in turn allowed the creation of fusion proteins made of fluorescent and host cell proteins. The GFP could thus be used as a reporter gene, which could monitor the expression of the gene it was fused to. Also the migration of the fusion proteins within the host cell could be traced yielding information on fundamental cell physiology (Chalfie *et al.* (1994), Piston *et al.* (2019b)).

The discovery of the GFP thus was the starting point of an new area of biological imaging as fluorescent proteins could now not only be used as a circulating contrast agent in morphological imaging, such as angiography, but functional imaging on the microscopic level was now possible allowing new ways to monitor cell physiology (Piston *et al.*, 2019b). To honour the relevance of this discovery, Osamu Shimomura, Martin Chalfie and Roger Y. Tsien were awareded the Nobel Prize in Chemistry 2008 “for the discovery and development of the green fluorescent protein, GFP” (NobelPrize.org, 2019).

From this point onwards began an ever ongoing development of fluorescent proteins (also known as fluorophores or fluorescent dyes) with tailored absorption and emission spectra and

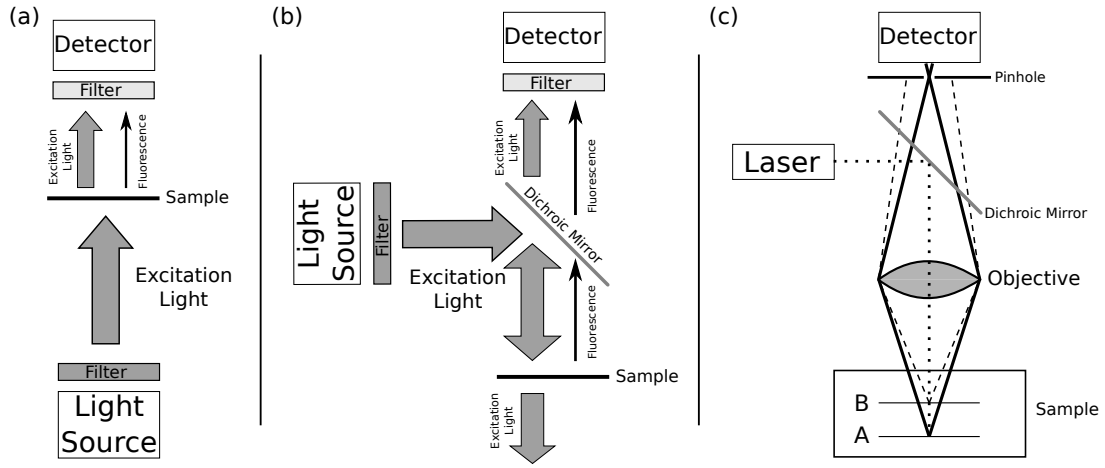

Figure 1.2: **Basic designs of fluorescence microscopes.** (a) Wide-field diascopic fluorescence microscopy. The sample is placed between light source and detector. (b) Wide-field episcopic fluorescence microscopy. Light source and detector are placed on the same side with respect to the sample using a dichroic mirror. (c) Laser scanning confocal fluorescence microscopy. A and B correspond to two exemplary planes of a sample, only plane A is in foucus. Adapted from Sanderson *et al.* (2014) (graphics program: Inkscape 0.91, opensource vector graphics editor, `http://www.inkscape.org`).

optimized properties for fluorescence imaging, such as the brightness level (Piston *et al.*, 2019a). Specific fusion proteins were developed combining fluorescent dyes with specific antibodies to monitor corresponding antigenes (Graves *et al.*, 2004). Fluorescent dyes were also combined with proteins binding hydroxyapatite to study osteoblastic activity (Zaheer *et al.*, 2001) to name just one other example.

1.1.3 Fluorescence Microscopy

Many different kinds of microscopes have been developed over the years to exploit the phenomenon of fluorescence and visualize labelled proteins to monitor their behaviour within cells. The very first fluorescence microscopes were based on a brightfield technique, which transmits light through the sample before it is collected by an objective to be observed by the eye and/or a detector, such as a camera (Abramowitz *et al.* (2019), Spring & Davidson (2019)).

But fluorescence is subject to a limited efficiency of converting an exciting photon into an emitted one, which is called the quantum yield (Cox, 2019). Also the emitted photons may be re-absorbed by the tissue sample on their way to being detected. This is why the fluorescence is very faint and has a much smaller intensity than the excitation light. Optical filters are therefore used to single out the fluorescent signal. These devices allow only the transmission of light of a certain wavelength spectrum, while other wavelengths contained within the light signal are absorbed. An optical filter applied to the light source can thus narrow the wavelength spectrum to the excitation wavelength of a given fluorescent dye to be imaged. And excitation photons not having interacted with the sample could be removed with a second optical filter located in front of the detector, which only transmits a wavelength spectrum fitted to the emission of the fluorescent dye. A basic design of such a *diascopic* microscope is shown in figure 1.2 (a). But as optical filters cannot select a single wavelength, the excitation light consists of a spectrum of

wavelengths that can possibly also include the emission spectrum of the fluorescent dye under consideration. This complicates the separation of the excitation and emitted light and is the main reason for the desire to develop fluorescent proteins with a large Stokes shift (Sanderson *et al.* (2014), Abramowitz *et al.* (2019)).

Another optical design was developed to improve the separation of the excitation and emitted light using a mirror, which reflects the former and transmitts the latter signal. This device is called a *dichroic mirror* and is placed between sample and detector at an angle of 45° to the sample/detector-axis. Excitation light entering the set up from the side can thus be reflected onto the sample to cause fluorescent emission. The excitation light is then partially reflected towards the detector superimposing the comparatively weak emitted light signal travelling in the same direction. While the emitted light is transmitted, light of all other wavelengths, including the excitation light, is reflected by the dichroic mirror. But similar to the above discussed filters, dichroic mirrors are not able to completely reflect or transmit light signals of a given wavelength. This is why the excitation light will also be partially transmitted and reach the detector. But the intensity difference between excitation and emitted light is dramatically reduced with this set up allowing for an improved separation of both signals. A basic design of such an *episcopic* microscope is shown in figure 1.2 (b) (Sanderson *et al.* (2014), Abramowitz *et al.* (2019)).

The standard wide-field fluorescence microscope applies light fitted to the exciation wavelength of a specific fluorescent dye to the entire sample. The advantage of this set up is that the whole sample can be examined simultaneously. But this technique is limited due to a thin plane of sharpest focus. Thus, labelled cell structures being out of focus will also be detected, which leads to a reduction of the microscope's resolution. This is especially problematic for thick samples with multiple layers of cells. This problem can be solved by using a laser scanning confocal fluorescence microscope (figure 1.2 (c)), which is able to remove fluorescent signals outside of the focal plane. Single points of a sample are scanned by the application of a laser at the excitation wavelength. Only the emitted light originating from the plane of focus is able to pass a pinhole aperture, which is placed in front of the detector. The final image is then created by combining the entire set of point measurements. A limitation of this method is the imaging speed, which is not only due to the compilation time of the single measurements. But it has also to do with the time that the laser is applied to a single point of the sample. While the application of a high-intensity laser would ideally enable the emission of a larger number of photons from the fluorescent dyes within a short amount of time, care must be taken not to destroy the fluorescent property of the fluorophore (known as photobleaching) let alone the sample by the application of too high energies (Sanderson *et al.* (2014), Cox (2019)).

The above discussed microscopes are three commonly used techniques to image fluorescent signals. A wide variety of other techniques have been developed in the past decades enabling deep insights into cell physiology even being able to reveal the presence of single molecules (Sanderson *et al.* (2014), Spring & Davidson (2019)).

1.1.4 Macroscopic Fluorescence Imaging

Fluorescence microscopy is especially suited to examine thin tissue preparations consisting of only a limited number of cell layers within *ex vivo*- or *in vitro*-studies. *In vivo*-studies are

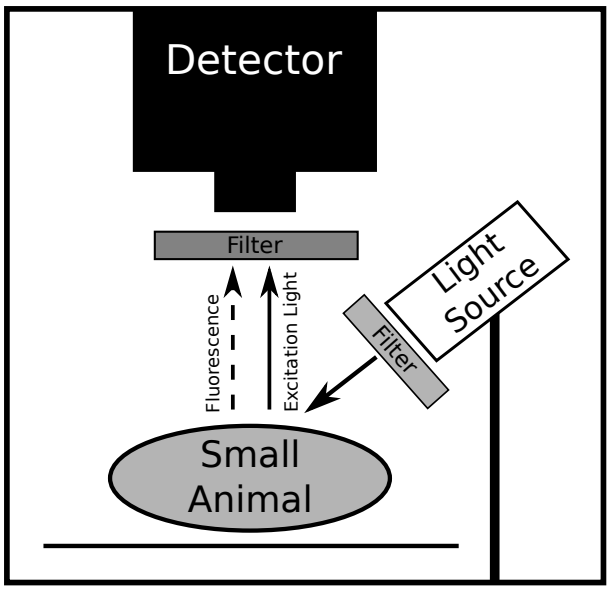

Figure 1.3: **Basic design of fluorescence reflectance imaging.** The excitation light is used to stimulate the fluorescent dye within the small animal, but it is also partly reflected and needs to be filtered in order to detect the resulting fluorescence. Adapted from Graves *et al.* (2004) (graphics program: Inkscape 0.91, opensource vector graphics editor, `http://www.inkscape.org`).

possible, but these are limited to examining processes occuring at a small animal's body surface, such as skin studies. Tissue located deeper than 500 μm below the surface cannot sensibly be resolved with fluorescence microscopy anymore. In order to image molecular processes *in vivo* within small animals therefore requires a different approach. X-ray and radioisotope imaging are only two of many common imaging techniques which have been successfully adjusted to preclinical small animal research. But it is the usage of non-ionising radiation in combination with the abundance of fluorescent dyes that makes the application of fluorescence so interesting in molecular imaging of small animals (Graves *et al.*, 2004).

Fluorescence reflectance imaging (FRI) is the most established technique in macroscopic fluorescence imaging. Similar to its microscopic equivalent, this technique either uses a light source with a broad spectrum, such as a tungsten lamp, in combination with an optical filter or it uses a laser. Both light sources are fitted to the excitation spectrum of a specific fluorescent dye with which a small animal is illuminated from above. After a fraction of these photons have reached and interacted with the fluorophores within the small animal's tissue, photons are re-emitted in a random direction (isotropically) partly travelling in the direction of the detector, which is also installed above the small animal (figure 1.3). The detected fluorescent signal is thus seemingly *reflected*. The detector is usually a camera containing a charge-coupled device (CCD) combined with a wide aperture objective to enable the detection of low intensity light signals. The resulting image is a two-dimensional planar representation of a three-dimensional subject. Information on how deep a fluorescent dye is located within a small animal is therefore only indirectly retrievable. Fluorescent signals are also affected by attenuation through absorption and scattering processes occuring within the tissue located between the fluorescent dye and the body surface (Wilson & Jacques, 1990). This limits the exploration of tissue located deeper

within a small animal. It is also more difficult to obtain quantitative information, such as the absolute level of dye concentration, which is responsible for the measured signal (Graves *et al.*, 2004).

A new technique has been developed in order to overcome these limitations and obtain quantitative information with macroscopic fluorescence imaging. It is called fluorescence molecular tomography (FMT) and reconstructs three-dimensional images from a set of two-dimensional planar images taken from different angles. It is therefore similar to computed tomography using X-rays. But the reconstruction algorithms are more complicated as the paths of the photons transmitted through the animal can not be considered to be straight lines, this is in contrast to higher energy X-rays. Efforts to improve the data aquisition and analysis are aimed to further enhance the reliability of these devices (Graves *et al.* (2004), Ntziachristos *et al.* (2005)).

1.2 Light Propagation in Biological Tissue

The attenuation of a light signal by biological tissue can be reduced to the most fundamental interaction of light with matter. The most common approach to describe this interaction in fields of applied physics, such as biophysics or medical physics, is the transport theory. It considers the interaction of each single photon of a light source with matter, such as a biological tissue. Maxwell's equations are an alternative focusing on the wave properties of light, but it was found that observations especially relevant to medical applications were better explained with the transport theory (Cheong *et al.*, 1990).

For the purpose of the project presented within the main part of this work and to describe the basic principles of the transport theory, the *light signal* (in units of *photon counts*) will be used as the physical parameter being attenuated by tissue. It is defined as the total number of photons being measured within a defined area of a camera's CCD-sensor (in units of *pixel* or mm^2) and exposure time (in units of *seconds*). It is a definition of the *light intensity* adapted to the specific circumstances of this project using an FRI-device. The *radiance* is the more exact defintion of the light intensity, which is therefore used within the differential equation describing the transport theory (Cheong *et al.*, 1990).

There are two underlying physical processes involved. On the one hand, the light signal is reduced by *absorption*. The energy of the photon is converted into another form, such as heat, during this kind of interaction with matter (Vogel, 1999). The absorption is represented by the absorption coefficient (μ_a) within the transport theory. This parameter describes the rate at which the light signal loses energy due to absorption with the distance travelled in tissue. The absorption in biological tissues is due to a variety of substances. Haemoglobin dominates the absorption for wavelengths below $600\,nm$ while water domintes it for wavelengths above $1300\,nm$. The absorption spectrum is at a minimum in between these wavelengths, called the *therapeutic window* (Wilson & Jacques, 1990).

A simple solution of the transport theory can be derived, if the entire attenuation of the light signal is only due to absorption. The solution reduces to the *Lambert-Beer Law* in this case yielding an exponential decay of the light signal (Φ) with the depth of tissue penetration (z):

$$\Phi(z) = \Phi_0\, e^{-\mu_a\, z}, \tag{1.1}$$

where Φ_0 corresponds to the unattenuated light signal (Cheong *et al.*, 1990).

In contrast to absorption, the photon energy is not converted into another form by light signal attenuation through *elastic scattering* from matter. The photon is simply deflected from its previous path by a certain angle (Vogel, 1999). This results in a number of photons not being able to be measured anymore depending on the specific angle of deflection and the size of the detector. This part of the light signal's attenuation is represented by the scattering coefficient (μ_s) within the transport theory. It is defined analogous to the absorption coefficient. While the "scattering in tissues is due to discontinuities in refractive index on the microscopic level, such as [...] collagen fibrils within the extracellular matrix" (Wilson & Jacques, 1990). Conglomerations of hydroxyapatite crystals are the major source of scattering in bone tissue (Firbank *et al.*, 1993).

A further parameter that describes the scattering properties of tissue is the anisotropy coefficient (g). It is the average cosine of the scattering angle and is applicable in tissue samples with multiple scattering events. These can be averaged to yield information on the general direction of the scattering pattern ranging from backwards ($g = -1$) via isotropic ($g = 0$) to forward scattering ($g = +1$). As an example, a value of $g = 0.5$ corresponds to forward scattering with an average deflection angle of $\theta = \arccos(0.5) = 60°$. A scattering event with $g = 0$ neither prefers backward nor forward scattering - the process is isotropic. Most biological tissues are highly forward scattering ($0.8 \leq g \leq 0.95$). This is why photons can travel deep into biological tissue and still be detectable. Even though they are scattered frequently, each photon is only deviated from its inital path by a small angle. The relatively low absorption in the therapeutic window further supports this effect (Cheong *et al.* (1990), Wilson & Jacques (1990) and Jacques (2013)).

The reduced scattering coefficient (μ_s') combines both of the above described scattering parameters. It is defined by a *similarity principle* and can thus be thought of as the scattering coefficient that would be observed, if the highly anisotropically scattering biological tissue (characterized by g and μ_s) was replaced by an isotropically scattering medium ($g' = 0$) keeping the measured light attenuation due to scattering constant (Cheong *et al.*, 1990):

$$\begin{aligned} \mu_s'(1 - g') &= \mu_s(1 - g) \\ \mu_s'(1 - 0) &= \mu_s(1 - g) \\ \mu_s' &= \mu_s(1 - g). \end{aligned} \tag{1.2}$$

The number of scattering events in this hypothetical medium is *reduced* in comparison to the biological tissue, just as the name of the parameter already implies. But the chances of a photon beeing detected after an isotropic scattering event is much smaller, which leads to a *similar* attenuation of the light signal compared to the one caused by the real biological tissue over all.

Jacques (2013) presents a simple expression for the reduced scattering coefficient, which allows sufficient predictions of light signal attenuation covering a large spectrum that includes

the wavelengths used within this project:

$$\mu_s'(\lambda) = a \left(\frac{\lambda}{500\,nm} \right)^{-b}, \tag{1.3}$$

where a corresponds to a scaling factor and b to the scattering power. A more complex equation, which considers the size of scattering structures compared to the wavelength of the interacting light signal (*Mie Scattering*: scattering structure $\geq$ signal wavelength. *Rayleigh Scattering*: scattering structure $<$ signal wavelength.), was found to yield comparable result.

The visible and near-infrared light spectrum is used within FRI. It has been shown that scattering dominates absorption in the majority of biological tissue within this spectrum (Wilson & Jacques, 1990). This is why the Lambert-Beer Law (equation 1.1) is not applicable. Solutions to the transport equation may lead to analytical expressions for the light signal attenuation in biological tissue. But these solutions are very complex and usually not suited for experimental research in biophysics due to the degree of measurement uncertainties. But approximations simplyfing these mathematical expressions are often sufficient for the purpose of predicting the light signal attenuation within biological tissue.

The *diffusion approximation* is a very widely used solution to the differential equation of the transport theory. But in order for this solution to be a sound approximation, several conditions need to be satisfied. First of all, scattering needs to dominate absorption. This has been proven by many previous projects and is especially true at the absorption minimum of the therapeutic window. Secondly, the scattering events need to be isotropic. Even though this is not the case within biological tissue, this condition is mathematically satisfied due to the definition of the reduced scattering coefficient introduced above. Thirdly, this approximation sufficiently predicts the attenuation of light signals only at a certain distance away from light sources and tissue boundaries. This results in the condition that the *mean free path*, which is the distance that a photon travels on average in between interactions with matter, needs to be smaller than the thickness of the tissue sample. The diffusion approximation then leads to a solution to the transport theory in which the light signal decays exponentially with z (based on Wilson & Jacques (1990)):

$$\Phi(z) \propto e^{-\mu\, z}, \tag{1.4}$$

where μ is the total attenuation coefficient due to absorption and scattering.

The light signal transmitted through a tissue sample is also altered at the interfaces between the surrounding medium (e.g. air) and the tissue sample itself. *Mismatched boundaries* between surroundings and tissue due to differing refractive indeces thus already lead to an attenuation of the light signal, which is not dependent on absorption or scattering events within the sample. On the one hand, *specular reflection* occurs at the air-tissue interface, which leads to an attenuation of the light signal before it has even entered the sample. On the other hand, *internal reflection* occurs at the tissue-air interface, leading to a loss of photons that have already passed through the sample (Wilson & Jacques, 1990).

Several attempts have been made in the past to examine the optical properties of different tissues and develop approaches to correct for the effect of attenuation on a light signal, this is summarized for example by Jacques (2013). A common technique involves the use of integrating

spheres. These spheres are hollow and their inside walls are coated with a highly scattering paint. A light source can be installed via small apertures in the walls of the spheres. The applied light is then uniformly scattered from the walls, this creates diffuse light (Kersten, 1983). A detector, which can also be installed in the walls, is then able to measure the light signal. Knowing the inside area of the spheres then enables to determine the total power of the light source. Usually two such spheres are used within experimental studies to measure optical properties of biological tissue. The sample is placed in the aperture that connects both spheres. A light source is installed only in the first sphere. Detectors, on the other hand, are installed in both. The fraction of light which remains within the first sphere can be detected in this way. It corresponds to the light signal reflected from the tissue sample. The light which is detected within the second sphere must have passed through the tissue sample, it corresponds to the transmitted light signal. The reflection and transmission measurements obtained with this set up are then converted into the desired optical tissue properties via a look up table that relates the measured data to the absorption and scattering coefficients. This look up table is usually generated by solving the transport equation numerically, i.e. using a computer algorithm, such as the Monte Carlo Method. Firbank *et al.* (1993) and Ugryumova *et al.* (2004)) have used this technique.

An alternative technique to determine optical tissue properties applies optical fibres. These can be used as a light source as well as a detection device to measure the attenuated light signal. For example, this technique can be applied to evaluate tissue properties during surgery (Bevilacqua *et al.*, 1999).

1.3 Correction Techniques

The limitations in studying molecular processes with FRI were discussed above. Apart from using FMT to overcome these limitations, correction techniques may be applied to data obtained with FRI in order to retrieve quantitative information, such as the concentration of a fluorescent dye accumulating in a given location within a small animal.

1.3.1 Uni-Modal Technique: Ratiometry

A great variety of different techniques to correct the measured light signal for attenuating effects was developed by exploiting additional information that can be retrieved from fluorescence imaging alone. These techniques are often based on a rule of proportion examining ratios between the total attenuated light signal and an additional parameter, for example the reflected excitation signal. This is the basic idea of *ratiometry*. One of these approaches uses two attenuated light signals each having a different wavelength. Information on tissue attenuation and the unattenuated light signals can be derived in this way (Bradley & Thorniley, 2006). In order to apply this technique to FRI, cells could be labelled with two fluorescent dyes emitting light of different wavelengths.

A simple example to clarify this approach is presented in the following. It assumes an experimental set up using a tissue sample with one tissue layer, which attenuates the light signal via absorption only. This leads to a set of two equations applying the Lambert-Beer Law

(equation 1.1):

$$\begin{aligned}\Phi_1(z) &= \Phi_0\, e^{-\mu_a(\lambda_1)\, z} = \Phi_0\, e^{-\mu_1\, z} \\ \Phi_2(z) &= \Phi_0\, e^{-\mu_a(\lambda_2)\, z} = \Phi_0\, e^{-\mu_2\, z},\end{aligned} \tag{1.5}$$

where the subscripts of the attenuated light signals (Φ) and the emission wavelengths (λ) refer to the first (1) and second (2) fluorescent dye. In a further simplification, the unattenuated light signal (Φ_0) is considered to be equal for both fluorescent dyes. This set of equations can then be solved for $-\mu_a\, z$, the ratio of which yields:

$$\begin{aligned}\frac{-\mu_1\, z}{-\mu_2\, z} &= \frac{\ln(\Phi_1) - \ln(\Phi_0)}{\ln(\Phi_2) - \ln(\Phi_0)} \\ \left(1 - \frac{\mu_1}{\mu_2}\right) \ln(\Phi_0) &= \ln(\Phi_1) - \frac{\mu_1}{\mu_2} \ln(\Phi_2)\,.\end{aligned} \tag{1.6}$$

This expression can finally be solved for Φ_0:

$$\Phi_0 = \exp\left(\frac{\ln(\Phi_1) - \frac{\mu_1}{\mu_2} \ln(\Phi_2)}{\left(1 - \frac{\mu_1}{\mu_2}\right)}\right). \tag{1.7}$$

Assuming prior knowledge of the wavelength-dependent attenuation coefficcient ($\mu_1/\mu_2 \neq 1$) therefore allows the calculation of the unattenuated light signal emitted by the fluorescent dyes.

This example shows that an already simplified experimental set up leads to an elaborate expression to correct light signals for tissue attenuation. And this expression gets even more complicated trying to deduce the concentration of the fluorescent dyes having accumulated in a specific sample region. As the emitted light does not only depend on the fluorophore concentration, but on the excitation light as well, the attenuation of the excitation light passing through the sample to reach the fluorescent dye needs to be considered as well. Furthermore, the quantum yield needs to be taken into account to determine the fluorophore concentration.

1.3.2 Multi-Modal Technique

1.3.2.1 Introduction to Micro-Computed Tomography

Micro-computed tomography (μCT) is an imaging technique which has become a standard in preclinical research. It was derived from computed tomography (CT), which was limited in resolution. But the usage of a micro-focus X-ray tube in combination with microscope optics then allowed the generation of high-resolution three-dimensional images of small animals (Baird & Taylor, 2017).

The basic principles of CT and μCT are the same. High-energy ionising radiation is produced via an X-ray tube. The applied voltage accelerates electrons creating a typical *Bremsstrahlung* upon interaction with a tungsten target (Vogel, 1999). This radiation consists of a broad spectrum of wavelengths. Photons with the highest energy are created, whenever the entire energy of a single accelrated electron is converted into a photon. This is why the X-ray energy is characterized by the voltage that is applied to the X-ray tube, which is usually set between 20 and 100 kVp ($kVp = peak\,voltage\,kilovolts$) for standard μCT-measurements in preclinical

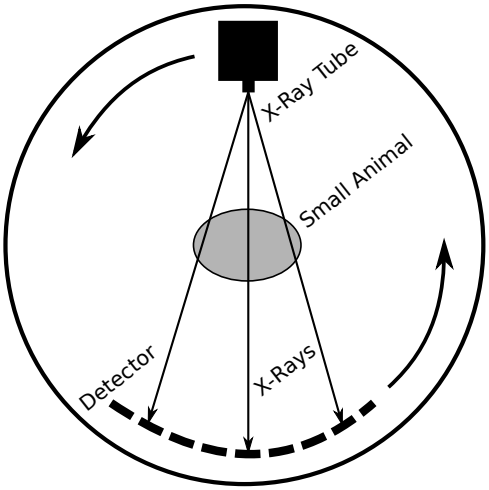

Figure 1.4: **Basic design of micro-computed tomography (μCT).** X-rays are produced with the X-ray tube and passed through the small animal sampling the attenuation of the different tissues. A two-dimensional image is recorded by an array of detectors. Different approaches exist concerning the angle of rotation of the X-ray tube, it is usually between 180° and 360°. The rotation of the array of detectors is synchronised with the X-ray tube. Stationary detectors are possible, if the array covers the entire area towards which the rotating X-ray tube points. Adapted from Prokop *et al.* (2003) (graphics program: Inkscape 0.91, opensource vector graphics editor, `http://www.inkscape.org`).

research. The X-ray beam is then shaped to a fan by a collimator before it passes through the subject under investigation. The attenuation of this signal dependes on the optical properties of the tissue, such as the atomic number or density, and the photon energies. While the low-energy X-rays are mostly absorbed, high-energy X-rays are mostly scattered. This results in a shift of the energy spectrum of the X-ray beam towards higher energies while passing through a subject. This is called *beam hardening*. As bone and soft tissue can be better differentiated with low-energy X-rays, filters are installed between the X-ray tube and the subject to remove the high-energy end of the X-ray spectrum. The attenuated X-ray beam is finally detected via a CCD-array as a two-dimensional planar image. Rotating the X-ray tube around the subject results in a vast collection of these two-dimensional images recorded from different angles (figure 1.4). Reconstruction algorithms are then applied to this data to generate a three-dimensional image which consists of units of small volumes (also known as volumetric pixels or voxels) each being assigned a specific attenuation parameter corresponding to the imaged tissue. A difference to CT is that the subject is rotated in some μCT-devices rather than the X-ray tube and array of detectors. But while this allows a simpler set up, it can only be sensibly applied for imaging *ex vivo*-samples (Prokop *et al.* (2003), Bouxsein *et al.* (2010), Boerckel *et al.* (2014), du Plessis *et al.* (2017)).

μCT-devices with a voxel size of 10 μm are especially interesting in the study of bone morphology in small animals, because it allows to resolve murine trabecular bone with width of approximately 30 to 50 μm. This non-destructive imaging technique has therefore become the gold standard in this field replacing histologic methods. Three-dimensional calculations are used to estimate the mean trabecular or cortical thickness with a sphere-fitting method. As the name of this method alread implies, virtual spheres are fitted in the volume occupied by bone

tissue within a selected region of the three-dimensional image (region of interest = ROI). The diameters of these spheres are then averaged to yield the mean thickness. It is also possible to determine the mineral density of bone tissue with μCT. The tissue mineral density (TMD) of a sepecific ROI is determined by averaging the attenuation data of voxels corresponding to bone tissue. The bone mineral density (BMD) also includes voxels corrponding to spaces in between trabecular structures containg bone marrow. These values can be expressed as a physical density (in units of $mg\ hydroxyapatite/cm^3 = mg\ HA/cm^3$) by calibration with a hydroxyapatite sample of known densities (Bouxsein *et al.*, 2010).

1.3.2.2 Correction Technique with Micro-Computed Tomography

An alternative to using a uni-modal technique to correct for tissue attenuation can be obtained from multi-modal imaging, which combines FRI- and μCT-measurements. Using the simplified model presented in chapter 1.3.1 again, which assumes a sample with a single tissue layer and absorption being the only relevant form of attenuation, the Lambert-Beer Law (equation 1.1) can simply be solved for the unattenuated light signal (Φ_0) to yield:

$$\begin{aligned} \Phi(z) &= \Phi_0\, e^{-\mu_a\, z} \\ \Phi_0 &= \Phi(z)\, e^{+\mu_a\, z}. \end{aligned} \tag{1.8}$$

Φ_0 could thus be estimated, if optical tissue properties (μ_a) were known and the attenuated light signal (Φ) and the tissue thickness (z) were determined with FRI and μCT respectively. A wavelength-dependence of the attenuation coefficient is not needed as only one fluorescent dye is used.

1.4 Aim of the Project

Fluorescence reflactance imaging is an established technique in preclinical research collecting mainly qualitative information, such as the location of pathologic events within small animal models. The acquisition of quantitative data is limited due to distorting attenuation effects. In order to gain a better understanding of the influence of biological tissue on light signals, studies have already been performed to characterise the attenuation coefficients of many different tissue types to be eventually able to correct the fluorescence for these distorting effects.

However, the experimental set up within these studies substantially differs from that of typical bio-molecular studies using FRI. As relevant differences were already found between the optical tissue properties of studies with a similar experimental set up (Cheong *et al.*, 1990), it was the aim of this project to derive an attenuation coeffcient more representative for studies on mice as carried out on today's molecular imaging devices.

This project specifically aimed to study the light signal attenuation in cortical bone tissue to enable the acquisition of quantitative data, such as the size of a tumor lesion within bone tissue. For this purpose, it had to be shown that differences in the light signal due to varying attenuation could be resolved with standard FRI-equipment used to perform bio-molecular research. This would allow the derivation of an attenuation coefficient specific to this set up.

Since there are quite a number of different impacting factors (e.g. reflection at interfaces, scattering at trabeculae, impact of the geometry of the specific experimental set up), exact correction of attenuation effects is difficult to achieve, but partial correction would already be very welcome to improve the interpretation of quantitative FRI.

The variations in the light signal attenuation due to bone tissue were analysed as a function of cortical thickness (d) and across a spectrum of signal wavelengths (λ) typically used for fluorescent labelling. Being able to resolve the thickness- and the wavelength-dependence of the light signal attenuation with FRI would enable the use of uni- and multi-modal correction techniques.

CHAPTER 2

Materials and Methods

2.1 Sample Preparation

Comparable to the projects of Firbank *et al.* (1993) or Ugryumova *et al.* (2004), *ex vivo*-preparations were used as bone samples. This enabled a better control over the cortical thickness compared to *in vivo*-measurements. Also complications due to multiple layers of tissues (investigated e.g. by Schmitt *et al.* (1990)) could thus be excluded. All experiments were carried out in accordance with the guidelines for Animal Care of Kiel University, this project was not an animal experiment in terms of the *Tierschutzgesetz der Bundesrepublik Deutschland* (TierSchG: §7 (2)). The bone samples were prepared from diaphyses of femora and tibiae of eight mice that were sacrificed prior to the realisation of this project.

All samples were chosen from mice with a physiological bone structure and mineralisation. After removing the soft tissue, small sections were cut from the diaphysis perpendicular to the main axis of the bone. This usually yielded one or two sections per bone. These cylindrical sections were then cut along a plane including the main axis of the bone. This resulted in bone samples with typical dimensions of approximately $3\,mm$ length and $1\,mm$ width (figure 2.1). Some samples were ground to further enlarge the range of the bone sample thickness. Abrasive paper was very carefully applied to these samples, but it turned out that samples with a geometry similar to the one shown in figure 2.2(a) were destroyed by the grinding process and were henceforth left unchanged. It was only possible to grind samples with a flat geometry (shown in figure 2.2(b)). Two samples could thus be added to the initial set of nine samples (sample 01 and 04, cf. table 3.1). As it was the aim of this project to study the optical properties of cortical bone tissue, it was ensured that non of the finally selected samples included trabecular bone, which would have distorted the measurement of the sample thickness. The samples were stored in phosphate buffered saline (PBS) at $-20^\circ C$ in between measurements.

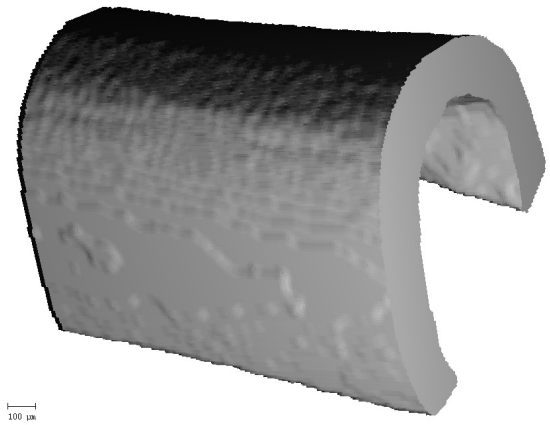

Figure 2.1: **Example of a three-dimensional reconstruction** obtained by scanning bone sample 11 with micro-computed tomography (cf. table 3.1) (graphics program accompanied by SCANCO VivaCT 40).

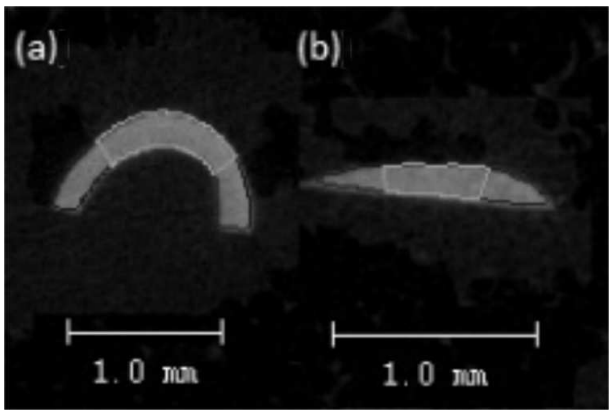

Figure 2.2: **Examples of reconstructed two-dimensional axial images obtained by micro-computed tomography (μCT).** Two exemplary bone samples with different geometries are presented: (a) sample 06; (b) sample 03 (cf. table 3.1). Bone properties were determined within the outlined contour of the 150 central μCT-slices of each bone sample (graphics program accompanied by SCANCO VivaCT 40).

2.2 Measurement of Tissue Properties with Micro-Computed Tomography

The cortical thickness (d) and the tissue mineral density (ρ_{TMD}) were determined with μCT (VivaCT 40, SCANCO Medical AG, Brüttisellen, Switzerland). Each of the eleven bone samples were individually scanned. For this purpose a single bone sample was wrapped in a thin cloth and inserted into a small plastic tube with an approximate diameter of 15 mm. This plastic tube could be tightly fastened within the μCT via a sample holder. This procedure prevented movements of the sample during the scan. The scans were then consecutively executed with a voltage of 70 kVp across the X-ray tube and a voxel size of 17.5 μm. The reconstruction of the scans then yielded a three-dimensional image of each bone sample. An example of these images can be seen in figure 2.1. More importantly, sets of two-dimensional axial images were reconstructed as well. Examples of these images are shown in figure 2.2.

Post processing of the reconstructed images was required before the desired cortical thickness and tissue mineral density could be derived from the μCT scans. Signal noise was reduced within the reconstruted images via a *Gaussian filter* first. The parameters of this filter had to be chosen carefully, as a set up ensuring maximum noise reduction would have resulted in a loss of contrast yielding blurred images without being able to differentiate bone from soft tissue anymore. The parameters set for the analysis of the entire μCT-data of this project were the following: *Size of the Gaussian kernel* = 2. *Standard deviation* (σ) = 0.8. The attenuation value above which a voxel would be counted as bone tissue was set in the next step. This parameter is known as the *threshold* and was set to 22 % of the maximum attenuation value for the analysis of the entire μCT-data of this project. A computer algorithm was then able to separate bone from other tissue applying this threshold, which is called *segmentation* (Bouxsein *et al.*, 2010). In the next step, contours were drawn to label the voxels containg the regions of bone cortex to be further analysed. The contouring was performed with another computer algorithm first. The result was then examined and adjusted manually wherever necessary within each single two-dimensional image. Only the 150 central μCT-slices of each bone sample (covering a distance of 2.6 mm) were used to calculate the desired sample properties. The focus was thus set on the part of the bone sample through which the light signals would pass on their way from the light source to the detector within the following attenuation measurements. This is also why only the central part of each bone sample's cross section was included in the contouring (shown in figure 2.2).

The signal attenuation caused by a single voxel is equal to an averaged value of each tissue type's attenuation contained within the specific voxel. This is why voxels representing an abrupt change in attenuation, for example at an interface between bone and air, distort the calculation of quantitative information, such as the tissue mineral density. This is a common artefact in CT-imaging and is called the *partial volume effect* (Prokop *et al.* (2003), Bushberg *et al.* (2012)). Another computer algorithm was therefore applied to the regions of interest of the reconstructed images removing a layer of one voxel from the outermost surface of the bone tissue, this procedure is called *peeling*. On the one hand, it ensures an accurate calculation of the tissue mineral density by excluding voxels representing non-mineralised tissue and air. On the other hand, there is a trade-off due to a possible distortion of the cortical thickness calculation. As this is done

with a *sphere-fitting method* (Bouxsein *et al.*, 2010), the resulting cortical thickness will be up to two voxel edge lengths thinner than without the peeling. But the contained bone tissue fraction within the surface voxels was assumed to be low due to chosing a low segmentation threshold. This is why the underestimation of the cortical thickness when applying the peeling was small compared to the overestimation of this parameter when not applying the peeling. A small underestimation of the cortical thickness was thus accepted to accurately calculate the tissue mineral density.

2.3 Attenuation Measurements

Ten different light emitting diodes (LEDs, Roithner Lasertechnik GmbH, Vienna, Austria) were chosen as light sources to simulate fluorescent signals. This had the advantage of ensuring constant unattenuated light signals and well defined wavelength spectra and signal sizes. The wavelength spectra of the LEDs were chosen to correspond to absorption and emission spectra of commonly used fluorescent dyes with peak wavelengths (λ) ranging from $\lambda = 470\,nm$ to $820\,nm$ (table 2.1). The LEDs were powered by a simple electric circuit (figure 2.3). An opto-mechanical device was then used to couple the emitted light into a glass fibre cable (components by THORLABS, Newton, USA with custom made modifications by the workshop of the Technical Faculty of Kiel University). This device was placed into a box impenetrable to light (figure 2.4 (a)). The glass fibre cable was then directed out of this box and into the FRI-device (NightOWL II, Berthold Technologies GmbH & Co.KG, Bad Wildbad, Germany). It was passed through a special port in a side wall of the measuring chamber ensuring that no stray light would enter the FRI-device during measurements. The end of the glass fibre cable was finally connected to the measuring bench (components also by THORLABS, Newton, USA with custom made modifications by the workshop of the Technical Faculty of Kiel University) installed beneath the FRI-device's CCD-camera (figure 2.4 (b)). Bone samples could thus be placed directly into the light path (figure 2.3). As the light signal was supplied by external LEDs, the excitation light supplied by the FRI-device was not needed.

Neutral density filters attenuate an incoming light signal without altering its wavelength spectrum. Chosing a combination of these filters (THORLABS, Newton, USA) along with a specific electric current applied to each LED and a specific exposure time (t) of the CCD-camera ensured that the light signal attenuated by the thinnest bone sample would not saturate the CCD-camera. As a further condition, the signal attenuated by the thickest sample still had to be detectable. Measurements of light signals without any attenuating bone samples ($\Phi_{0,\lambda}$) would have led to the saturation of the CCD-camera, if these settings had been used. Therefore, the unattenuated signals were measured with an exposure time reduced by two orders of magnitude ($t = 100\,ms$ instead of $t = 10\,s$).

2.3.1 Light Signal Measurements with Varying Exposure Time

It was analysed in preliminary measurements whether an unattenuated light signal ($\Phi_\lambda(t)$) measured at $t = 100\,ms$ could be extrapolated to calculate $\Phi_\lambda(t = 10\,s)$. This would allow the application of a shorter exposure time ($t = 100\,ms$) to determine the unattenuated light signal

Table 2.1: **Peak wavelengths of light emitting diodes (LEDs)** used within this project are matched with absorption and/or emission spectra of commonly used fluorescent dyes. Further properties of the LEDs can be found in corresponding data sheets on the LED-supplier's website listed by part number (Roithner Lasertechnik GmbH, 2020). Further properties of the fluorescent dyes can be found in the corresponding references.

LED		**Fluorescent Dye**			
Part Number	**Peak Wavelength (in *nm*)**	**Name**	**Wavelength Spectrum**	**Peak Wavelength (in *nm*)**	**Reference**
B5B-437-IX	470	Green Fluorescent Protein (GFP)	Absorption	470 (minor)	Chalfie *et al.* (1994)
B5B-433-B505	505	GFP	Emission	509	Chalfie *et al.* (1994)
B5B-433-014	570	DsRed2	Absorption	563	Shcherbo *et al.* (2007)
LED590-03	590	DsRed2	Emission	588	Shcherbo *et al.* (2007)
		Katushka	Absorption	588	Shcherbo *et al.* (2007)
ELD-650-523	650	Katushka	Emission	635	Shcherbo *et al.* (2007)
LED680-02AU	680	Infrared Fluorescent Protein (IFP)	Absorption	684	Shu *et al.* (2009)
		Near-Infrared Fluorescent Protein (iRFP)	Absorption	690	Filonov *et al.* (2011)
LED710-01AU	710	IFP	Emission	708	Shu *et al.* (2009)
		iRFP	Emission	713	Filonov *et al.* (2011)
LED750-03AU	750	Osteosense® 750 EX	Absorption	749	PerkinElmer (2010a)
LED780-03AU	780	Osteosense® 750 EX	Emission	770	PerkinElmer (2010a)
		Indocyanine Green (ICG)	Absorption	778	Polom *et al.* (2011) Desmettre *et al.* (2000)
		Osteosense® 800	Absorption	780	PerkinElmer (2010b)
LED820-01AU	820	Osteosense® 800	Emission	805	PerkinElmer (2010b)
		ICG	Emission	830	Polom *et al.* (2011) Desmettre *et al.* (2000)

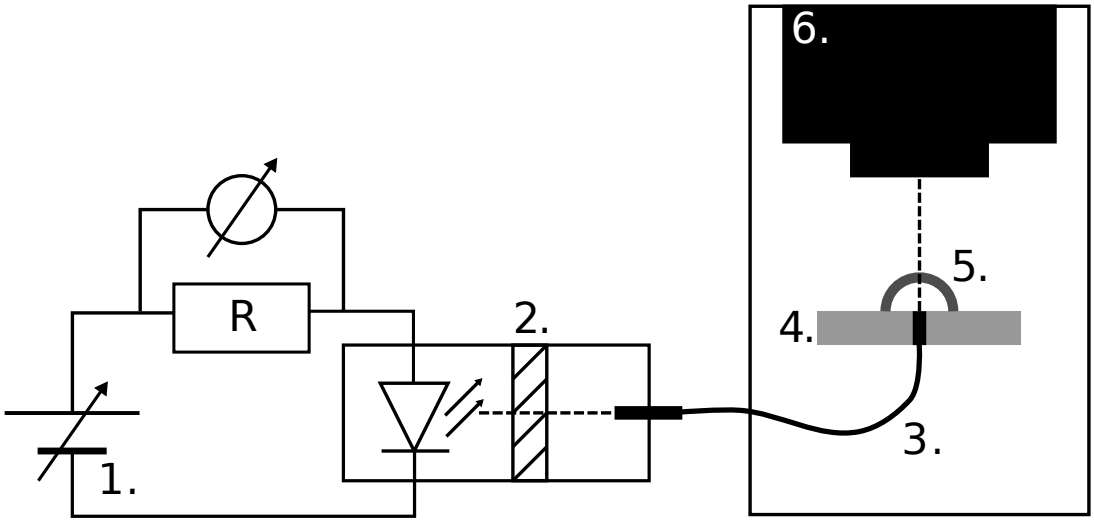

Figure 2.3: **Illustration of experimental set up:** 1. - electric circuit with power source, resistor ($R = 1\ k\Omega$), voltmeter and light emitting diode; 2. - opto-mechanical coupling device with neutral density filter; 3. - glass fibre cable; 4. - measuring bench; 5. - bone sample; 6. - fluorescence reflectance imaging-device with charge-coupled device-camera (graphics program: Inkscape 0.91, opensource vector graphics editor, `http://www.inkscape.org`).

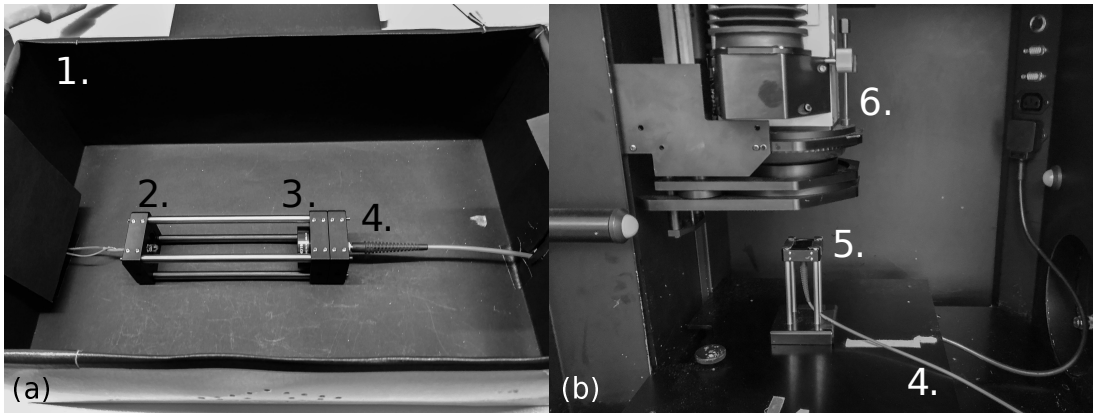

Figure 2.4: **Photographs of experimental set up.** The opto-mechanical coupling device can be seen in photograph (a). It is placed inside a box (1.) impenetrable to light (lid removed) and consists of an electrically powered light emitting diode (2., Roithner Lasertechnik GmbH, Vienna, Austria), a neutral density filter (3., THORLABS, Newton, USA) and one end of a glass fibre cable (4., THORLABS, Newton, USA). The experimental set up within the interior of the fluorescence reflectance imaging-device (NightOWL II, Berthold Technologies GmbH & Co.KG, Bad Wildbad, Germany) can be seen in photograph (b). The other end of the glass fibre cable (4.) is connected to the measuring bench (5., components by THORLABS, Newton, USA with custom made modifications by the workshop of the Technical Faculty of Kiel University), which is placed directly below the charge-coupled device-camera (6.) of the fluorescence reflectance imaging-device (graphics program: Inkscape 0.91, opensource vector graphics editor, `http://www.inkscape.org`).

Table 2.2: **Set up of the electrical circuit and the opto-mechanical equipment for the extrapolation and attenuation measurements.** The optical density refers to the attenuation of the light signal caused by the neutral density filters used.

LED Peak Wavelength (in nm)	**Extrapolation Measurements**		**Attenuation Measurements**	
	Optical Density	**Applied Current (in mA)**	**Optical Density**	**Applied Current (in mA)**
470	10^{-5}	4.0	10^{-3}	2.7
505	10^{-5}	4.0	10^{-3}	2.3
570	10^{-3}	1.3	10^{-1}	2.7
590	10^{-4}	1.7	10^{-2}	3.1
650	10^{-5}	5.0	10^{-3}	6.2
680	10^{-5}	3.5	10^{-3}	4.1
710	10^{-5}	4.0	10^{-3}	4.4
750	10^{-5}	2.0	10^{-3}	3.4
780	10^{-5}	2.0	10^{-3}	3.8
820	10^{-5}	2.7	10^{-3}	3.5

illuminating a bone sample ($\Phi_{0,\lambda} = \Phi_\lambda(t = 10\,s)$) within the main attenuation measurements. For this purpose, the behaviour of $\Phi_\lambda(t)$ was examined for each wavelength spectrum with varying exposure times ranging from $t = 100\,ms$ to $t = 10\,s$.

Ten sets of measurements were performed, one set for each signal wavelength spectrum. A combination of the electric current powering a specific LED and neutral density filters was chosen for each set to ensure that a signal could be differentiated from background noise for $t = 100\,ms$ as well as to prevent saturation of the CCD-camera for $t = 10\,s$. The specific set up is presented in table 2.2. Within each set of measurements $\Phi_\lambda(t)$ was then consecutively measured using five different values of $t = \{100\,ms;\ 500\,ms;\ 1\,s;\ 5\,s;\ 10\,s\}$. This procedure was repeated another two times to complete one set of measurements.

The raw data of the preliminary measurements thus consisted of light signal measurements performed three times for every combination of λ and t. In order to allow the extrapolation of an unattenuated light signal within the main measurements, it had to be shown that a change in t would lead to a proportional change in $\Phi_\lambda(t)$. The data was therefore analysed with a linear regression model, one for each λ:

$$\Phi_\lambda(t) = \alpha_\lambda t + \beta_\lambda\ , \tag{2.1}$$

where α_λ and β_λ correspond to the slope and the intercept-term of the linear regression model respectively.

2.3.2 Main Experimental Study

The *main experimental study* was divided into ten subsets of measurements with equal measuring procedures, one subset for each signal wavelength spectrum. The unattenuated light signal ($\Phi_{0,\lambda}$) was determined within these subsets first by taking a measurement without an attenuating bone sample placed on top of the measuring bench. The electrical current powering the specific LED as well as the optical filters were not changed for the entire subset of measurements (table 2.2). This ensured a constant sample illumination. The bone samples were then consecutively placed on

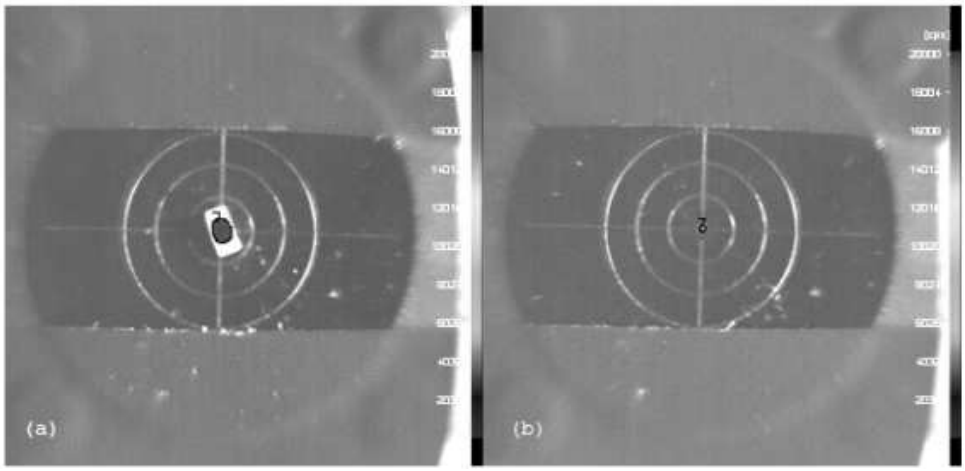

Figure 2.5: **Examples of photographs combined with signal images as overlays:** (a) with bone sample; (b) without bone sample (graphics program: indiGO, Berthold Technologies).

top of the measuring bench inside the imaging device. Photographs and signal images were then taken. The measuring chamber was illuminated with white light to take the photographs. The signal images recorded only the light originating from the LEDs, these were presented as overlays on the corresponding photographs by the analysis software accompanied with the NightOWL (indiGO, Berthold Technologies GmbH & Co.KG, Bad Wildbad, Germany). Examples of these combined images are shown in figure 2.5. A single measurement was only accepted if the part of the bone sample previously analysed with the μCT was well centred on the measuring bench directly above the end of the glass fibre. Otherwise the measurement was rejected. The decision was based on the photographic image. A cross hair on the top surface of the measuring bench, which can also been seen in figure 2.5, improved the accuracy and precision of this decision. Once one measurement was accepted for each of the 11 bone samples, $\Phi_{0,\lambda}$ was determined again. The constant illumination was thus reassured. This procedure was repeated four times to complete one subset of measurements. The total number of measurements acquired within the main experimental study (n) thus added up to 440.

2.3.3 Modified Set Up Study

Measured optical data may also depend on the experimental set up (Cheong *et al.*, 1990). In order to not only be able to compare the results of the main experimental study with literature values, a second study was performed to test the sensitivity of findings to potential changes in the experimental set up as well, the *modified set up study*. It was conducted by a different operator. Additionally, the CCD-camera of the FRI-device had to be exhanged due to technical issues introducing a major change that was - to this degree - not initially planed. It resulted in a different geometrical set up with an additional distance between the measuring bench and the CCD-camera of approximately $5\,cm$ (relative change in comparison to the set up of the main experimental study $\approx 50\,\%$) in order to focus the CCD-camera on the top surface of the measuring bench (cf. figure 2.3). Consequently, the unattenuated light signal ($\Phi_{0,\lambda}$) had to be adjusted to meet the already outlined conditions to not only prevent the CCD-camera from saturation but also be able to detect the light signals attenuated by the thickest bone sample.

Compared to the main experimental study fewer LEDs (including 7 of the original 10 peak signal wavelengths (cf. table 2.1, in nm): 470, 505, 590, 680, 750, 780, 820) and fewer bone samples (including 6 of the original 11 bone samples with sample numbers (cf. table 3.1): 01, 02, 04, 06, 08, 10) were used for this modified set up study. Also, the attenuated light signal was only measured once for every combination of bone sample and LED used. Therefore, the total number of measurements acquired with this study (n) added up to 42.

2.4 Modelling the Attenuation

The signal images were analysed with the indiGO software (Berthold Technologies GmbH & Co.KG, Bad Wildbad, Germany). A peak search function was performed first. It singled out the signal area to be further analysed. The lower threshold required to include a pixel in the signal area was set to 40 photon counts. This ensured a reduction of background noise. The raw data included the integral of the photon count of a single pixel over the signal area and the exposure time. Reference to this variable is made whenever mentioning the *light signal* (in *photon counts*) in the following.

The completion of all ten subsets of measurements of the main experimental study yielded the raw data with four measurements of the attenuated light signal for every combination of bone sample and signal wavelength. This became the basis of the statistical analysis from which the desired optical properties of the bone samples were determined. A similar procedure applies to the modified set up study.

2.4.1 Univariate Regression Analyses

The above described subsets governing the measuring procedure were kept for an initial analysis of the data to examine the light signal's behaviour when only varying the bone sample. All data points having been measured with the same signal wavelength thus remained in one of the ten subsets. Each of these subsets was then analysed separately with a simple linear univariate regression model focusing on the behaviour of the light signal with varying sample thickness (d):

$$\ln\left(\frac{\Phi_\lambda(d)}{\Phi_{0,\lambda}}\right) = c - \mu_d\, d, \tag{2.2}$$

where $\Phi_\lambda(d)$ corresponds to the light signal of a specific λ-subset having been attenuated by a bone sample with cortical thickness d. $\Phi_{0,\lambda}$ is the extrapolated, unattenuated light signal. The ratio $\Phi_\lambda(d)/\Phi_{0,\lambda}$ normalises the dependent variable in equation 2.2. The regression model thus describes the *fraction* of the light signal passing through the bone sample and is independent of the strength of the unattenuated light signal ($\Phi_{0,\lambda}$), which is different for every λ. This procedure allowed the inclusion of the data of all wavelengths to be compared within a single multivariate regression model, which is presented below. An exponential decay of the light signal with increasing bone sample thickness was expected on the basis of the theoretical background presented in chapter 1.2. The logarithm was applied to the regression model to simplify the calculations of the optical properties of bone tissue, such as μ_d, which is the attenuation coefficient of this univariate regression model. The parameter c is a constant, its meaning will be further

analysed in the following multivariate regression model.

The data was then rearranged into different subsets in a second step to examine the light signal's behaviour when only varying the signal wavelength. All data points having been measured with the same bone sample were assigned to one of eleven new subsets. Each of these subsets was then analysed separately with another simple linear univariate regression model focusing on the behaviour of the light signal with varying peak wavelength (λ):

$$\ln\left(\frac{\Phi_d(\lambda)}{\Phi_{0,\lambda}}\right) = c - \mu_\lambda\,\lambda, \tag{2.3}$$

where $\Phi_d(\lambda)$ corresponds to the attenuated light signal of a specific bone sample-subset using an LED with peak wavelength λ. The attenuation coefficient μ_λ and the constant c are chosen in analogy to the univariate regression model presented in equation 2.2.

2.4.2 Multivariate Regression Analyses

The multivariate regression model used in this project is based upon the diffusion approximation of the radiative transport theory (chapter 1.2). It is an exponential expression, which relates the attenuated light signal (Φ) to d and λ. The experimental set up satisfies all conditions required for the application of this approximation. First of all, the use of the reduced scattering coefficient (μ_s') introduces the mathematical equivalent of isotropic scattering of an actually highly anisotropically scattering occuring in biological tissue (Cheong *et al.*, 1990). Secondly, the dominance of scattering over absorption within biological tissue was confirmed by many previous projects, some of which are summarized by Cheong *et al.* (1990). And finally, even the thinnest bone sample used ($d = 126\,\mu m$) was thicker than the average distance which photons need to travel within biological tissue in between scattering events (known as the *mean free path*, $mfp \ll 100\,\mu m$), these events can therefore be approximated as being distant from sample boundaries. By definition, the reduced scattering coefficient does not only contain information on the number of scattering events within tissue but on the average scattering angle as well (chapter 1.2). It can only be utilized, if multiple scattering events occur during a photon's path through the bone sample. This was also ensured by choosing bone samples with $mfp \ll d$ (Jacques (2013), Wilson & Jacques (1990)).

As was already stated above, it has been shown that scattering dominates absorption within the wavelength spectrum commonly used for FRI (Cheong *et al.*, 1990). But an even smaller influence of the absorption on the total attenuation of the light signal was expected within the current project as the *ex vivo*-preparations were lacking blood and therefore also haemoglobin, which is one of the strongest sources of absorption in biological tissue (Jacques, 2013). And as the equipment was not designed to determine the absorption and scattering coefficients separately, as it can be done with the equipment used by Firbank *et al.* (1993) or Ugryumova *et al.* (2004), a differentiation between absorption and scattering processes causing the total attenuation is not possible. The absorption is therefore neglected by approximating the total attenuation coefficient (μ) as

$$\mu \approx \mu_s' \quad for \quad \mu_s' \gg \mu_a. \tag{2.4}$$

Finally, an exponential expression on the basis of the diffusion approximation to the radiative

transport theory (cf. equation 1.4, Wilson & Jacques (1990)) with further modifications to adapt to the special needs of the FRI-set up was used to create a non-linear regression model to fit the data obtained with this project:

$$\Phi(d,\lambda) = \Phi_{0,\lambda}\, K(\lambda)\, e^{-\mu(\lambda)\, d}, \tag{2.5}$$

where

$$\mu(\lambda) \approx \mu_s'(\lambda) = a \left(\frac{\lambda}{505\, nm} \right)^{-b} \tag{2.6}$$

and

$$K(\lambda) = K_0 + \Delta K \left(\frac{\lambda}{505\, nm} \right) \tag{2.7}$$

leads to

$$\ln\left(\frac{\Phi(d,\lambda)}{\Phi_{0,\lambda}} \right) = \ln\left(K_0 + \Delta K \left(\frac{\lambda}{505\, nm} \right) \right) - a \left(\frac{\lambda}{505\, nm} \right)^{-b} d. \tag{2.8}$$

The specific expression for the reduced scattering coefficient (μ_s', equation 2.6) was adapted from Jacques (2013) using a scaling factor (a), the scattering power (b) and a reference wavelength of $505\, nm$, which corresponds to the peak wavelength of one LED used within this project (cf. table 2.1). The ratio $\Phi(d,\lambda)/\Phi_{0,\lambda}$ normalises the dependent variable in equation 2.8 again allowing the inclusion of the data of all wavelengths to be compared within one regression model. The logarithm was applied to the regression model to simplify the calculations of the optical properties of bone tissue, such as μ.

The variable K (in reference to Wilson & Jacques (1990)) was introduced to account for other influences reducing the light signal being wavelength-dependent but bone thickness-independent, such as reflection at interfaces, where K_0 and ΔK refer to the intercept-term and slope of a linear function with respect to λ respectively (equation 2.7). For the major part, K accounts for the attenuation of the light signal due to specular reflection, which occurs at the air-bone interface, and internal reflection, which occurs at the bone-air interface (Wilson & Jacques, 1990). This is particularly important in the presence of mismatched boundaries, where the refractive index of the surrounding medium is much different to the one of the tissue sample itself (cf. chapter 1.2). This was the case in the current project with air as the surrounding medium. Via dispersion (Vogel, 1999), K thus depends on λ. But this parameter is also influenced by other factors, such as the surface roughness or the angle of illumination of the sample (Wilson & Jacques, 1990). Most of these factors can not easily be controlled with an experimental set up but will rather tend to always randomly influence the attenuation especially in future *in vivo*-measurements.

2.4.3 Comparison of the Reduced Scattering Coefficients

A data set combining both studies of this project was used to test whether there exists a statistically significant difference between the two reduced scattering coefficients derived from each study separately. The variable Ω was introduced into the multivariate regression model for this purpose. It is a dichotomous variable, which specifies the operator having taken the measurents. $\Omega = 1$ thus refers to data of the main experimental study, $\Omega = 2$ refers to data of the modified set up study. Theoretically, the initial model presented in equation 2.8 could

have been used here as a basis. But to keep the following expression as simple as possible, the only variables used were the ones showing a statistically significant effect on the light signal attenuation within the main experimental study as presented in chapter 3.3.2:

$$\ln\left(\frac{\Phi(d,\Omega)}{\Phi_{0,\lambda}}\right) = \ln(K_0) - a\,d + c_\Omega\,\Omega + c_{d,\Omega}\,d\,\Omega, \tag{2.9}$$

where c_Ω and $c_{d,\Omega}$ are the coefficients of the variables Ω and $d\,\Omega$ respectively. This model can be rewritten as follows to clarify the relationship between Ω and the attenuation coefficient of this regression model (μ^*):

$$\begin{aligned}
\frac{\Phi(d,\Omega)}{\Phi_{0,\lambda}} &= e^{\ln(K_0) - a\,d + c_\Omega\,\Omega + c_{d,\Omega}\,d\,\Omega} \\
\Phi(d,\Omega) &= \Phi_{0,\lambda}\,K_0\,e^{-a\,d + c_\Omega\,\Omega + c_{d,\Omega}\,d\,\Omega} \\
\Phi(d,\Omega) &= \Phi_{0,\lambda}\,K_0\,e^{-(a - c_{d,\Omega}\,\Omega)\,d + c_\Omega\,\Omega} \\
\Phi(d,\Omega) &= \Phi_{0,\lambda}\,K_0\,e^{-\mu^*\,d + c_\Omega\,\Omega},
\end{aligned} \tag{2.10}$$

where μ^* is defined as the coefficient of d within the exponential expression of this combined regression model:

$$\mu^* = a - c_{d,\Omega}\,\Omega. \tag{2.11}$$

$c_{d,\Omega}$ thus influences μ^*. A test for the statistical significance of $d\,\Omega$ therefore allows to evaluate the influence of the experimental set up on the attenuation coefficients of the two studies of this project.

2.5 Statistical Analyses

All analyses were carried out with *JMP 5.0.1* software (SAS Institute, Cary, North Carolina, USA). *Standard error* refers to the standard error of the mean. Associations were modelled by linear and non-linear regression models of the light signal and its logarithm.

CHAPTER 3

Results

3.1 Cortical Thickness and Tissue Mineral Density

The μCT-measurements of the eleven bone samples yielded d as well as ρ_{TMD}. The results are summarized in table 3.1 and range from $126\,\mu m$ to $239\,\mu m$ and from $909\,mg$ *hydroxyapatite per* cm^3 ($mg\,HA/cm^3$) to $1103\,mg\,HA/cm^3$ respectively. It was found that the inter-bone variability of the tissue mineral density is small. It shows a mean value of $998\,mg\,HA/cm^3$ and an 95 % confidence interval of $\pm\,42\,mg\,HA/cm^3$ around the mean. The tissue mineral density was therefore considered constant within the physiologically structured and mineralised bone samples used and neglected as an independent variable within the regression models.

3.2 Light Signal and Exposure Time

The measurements examining the behaviour of $\Phi_\lambda(t)$ with varying exposure time were analysed with the linear regression model introduced in equation 2.1. A statistically significant influence of the intercept-term (β_λ) could not be shown for eight of the ten measurement subsets (table 3.2). Only the subsets using the signal wavelength $\lambda = 590\,nm$ and $\lambda = 750\,nm$ yielded a p-value for β_λ above the 5 %-significance level. But the 95 %-confidence intervals (CI_{95}) of these two intercept-terms were very close to zero (CI_{95} for β_λ at $\lambda = 590\,nm$: $-31710\,photon\,counts \leq CI_{95} \leq -2085\,photon\,counts$, CI_{95} for β_λ at $\lambda = 750\,nm$: $-32967\,photon\,counts \leq CI_{95} \leq -4479\,photon\,counts$). In comparison with the number of photons having been measured within one second (which is equal to the slope, α_λ) both of the concerned intercept-terms are negligibly small, this is visualised by figure 3.1. Therefore, $\Phi_\lambda(t)$ was considered to be proportional to t for the exposure times used within this project ($100\,ms \leq t \leq 10\,s$). It was therefore possible to extrapolate $\Phi_\lambda(t = 100\,ms)$ to determine $\Phi_\lambda(t = 10\,s) = \Phi_{0,\lambda}$, the unattenuated light signal illuminating the bone samples within the main attenuation measurements.

Table 3.1: **Summary of bone sample properties determined with micro-computed tomography (μCT).** The cortical thickness (d) and the tissue mineral density (ρ_{TMD}) of the 11 bone samples were determined with μCT. Samples 01 and 04 were ground during the preparation process (corresponding sample numbers and properties are written in bold face).

Sample Number	**d in μm (Standard Deviation)**	**ρ_{TMD} in $mgHA/cm^3$**
01	**126 (25)**	**1004**
02	138 (19)	1003
03	143 (22)	926
04	**161 (34)**	**1049**
05	166 (25)	921
06	184 (23)	1070
07	188 (23)	992
08	189 (33)	1019
09	202 (18)	980
10	209 (33)	909
11	239 (23)	1103

Table 3.2: **Summary of preliminary light signal measurements with varying exposure time** using linear regression to model the light signal ($\Phi_\lambda(t)$) for each signal wavelength (λ). The coefficients of the linear regression model, α_λ and β_λ, correspond to the slope and the intercept-term respectively. *Std.Error* refers to the standard error of the mean.

λ in nm	**Coefficient of Determination (R^2)**	**Estimate of $\alpha_\lambda \pm$ *Std.Error* in *photon counts per sec.* (p-value)**	**Estimate of $\beta_\lambda \pm$ *Std.Error* in *photon counts* (p-value)**
470	0.96	73825 ± 3904 (< 0.001)	-3004 ± 19618 (0.881)
505	0.98	67879 ± 2444 (< 0.001)	4184 ± 12283 (0.739)
570	1.00	103148 ± 1738 (< 0.001)	-17357 ± 8735 (0.068)
590	1.00	110240 ± 1504 (< 0.001)	-16898 ± 7557 (0.044)
650	0.94	99414 ± 7247 (< 0.001)	-3664 ± 36418 (0.921)
680	0.98	96542 ± 3966 (< 0.001)	-540 ± 19929 (0.979)
710	1.00	124409 ± 1505 (< 0.001)	-9578 ± 7562 (0.228)
750	1.00	137534 ± 1446 (< 0.001)	-18723 ± 7267 (0.023)
780	1.00	106926 ± 1679 (< 0.001)	2897 ± 8437 (0.737)
820	0.99	122567 ± 3415 (< 0.001)	-19542 ± 17161 (0.275)

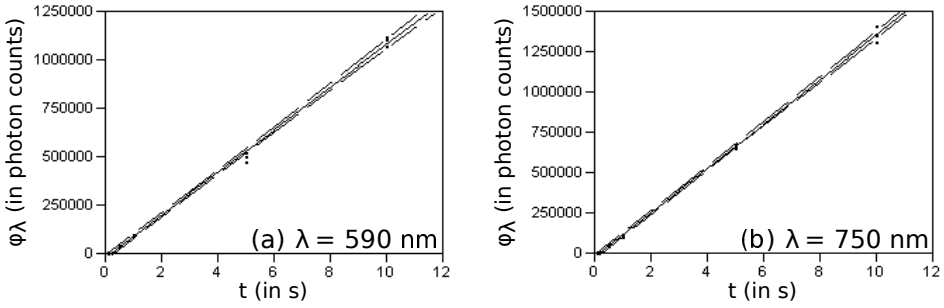

Figure 3.1: **Scatter plots and superimposed linear regression model of data subsets of preliminary light signal measurements with varying exposure time and constant signal wavelength.** The light signal signal (Φ_λ) is plotted against the exposure time (t) at the following signal wavelengths (λ): (a) $590\,nm$; (b) $750\,nm$. The corresponding linear regression model is superimposed on each scatter plot together with confidence curves to the 5%-significance level (graphs produced with JMP 5.0.1, modified with Inkscape 0.91, opensource vector graphics editor, `http://www.inkscape.org`).

3.3 The Attenuation Coefficient

3.3.1 Univariate Regression Analyses

The attenuation data arranged in subsets of equal signal wavelength is presented in figure 3.2 and 3.3. On first sight, the scatter-plots show a moderate spread with a clear decline of the light signal with increasing cortical thickness in most of the subsets. These results were verified with univariate regression analyses based on the model introduced in equation 2.2 and summarized in table 3.3. An exponential decay of the light signal with increasing cortical thickness could be shown in nine of the ten subsets. This correlation was not strong enough only for the $\lambda = 470\,nm$-subset yielding the lowest coefficient of determination of all subsets and a p-value above the 5 %-significance level. These findings imply a relevant influence of the cortical thickness on the multivariate regression model, while the spread of the scatter-plots in combination with the moderate coefficients of determination might relate to the existence of other influences not being accounted for with this univariate regression model. The attenuation data which was rearranged in subsets of equal cortical thickness is presented in figure 3.4 and 3.5. The scatter-plots show a wide spread of the data points. A correlation between the light signal and the signal wavelength could visually not be detected in at least half of the presented subsets ((e) $d = 166\,\mu m$, (g) $d = 188\,\mu m$, (h) $d = 189\,\mu m$, (i) $d = 202\,\mu m$ and (j) $d = 209\,\mu m$). The distributions of the data points within the other subsets are not significantly clearer. These results are supported by the superimposed univariate regression model introduced in equation 2.3. The summary of the regression analyses are presented in table 3.4. No relevant correlation was found between the light signal and the signal wavelength in any of the subsets yielding a maximum coefficient of determination of 0.06. The estimated values of the attenuation coefficient of each subset (μ_λ) were found to be positive for two subsets and negative for the rest. This variability is in line with the p-values, which are all well above the 5 %-significance level. These

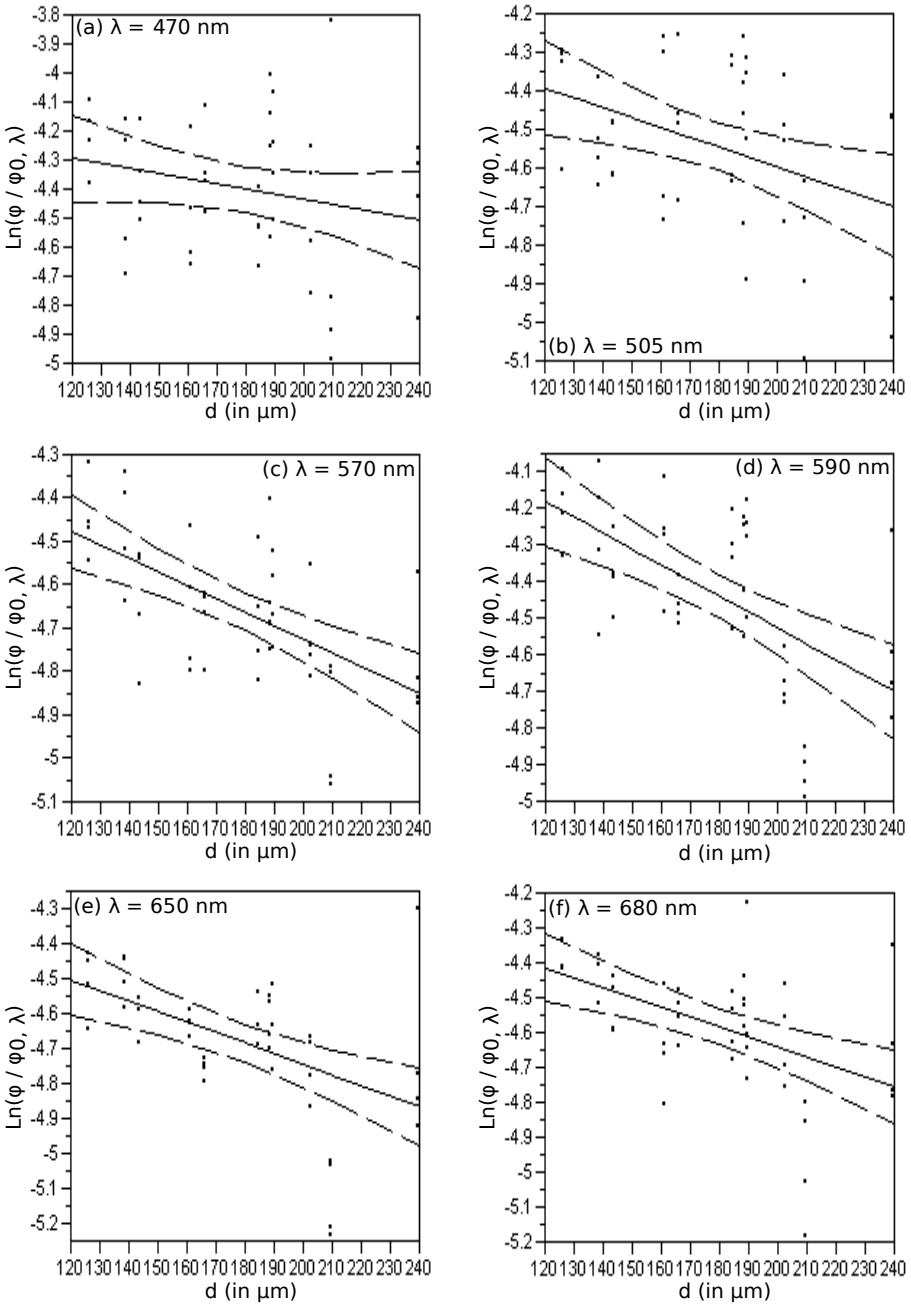

Figure 3.2: **Scatter plots and superimposed univariate regression model of data subsets of the main experimental study with varying cortical thickness and constant signal wavelength.** The natural logarithm of the normalised, attenuated light signal ($\ln(\Phi/\Phi_{0,\lambda})$) is plotted against the cortical thickness (d) at the following signal wavelengths (λ): (a) $470\,nm$; (b) $505\,nm$; (c) $570\,nm$; (d) $590\,nm$; (e) $650\,nm$; (f) $680\,nm$. The corresponding linear univariate regression model is superimposed on each scatter plot together with confidence curves to the 5%-significance level (graphs produced with JMP 5.0.1, modified with Inkscape 0.91, opensource vector graphics editor, `http://www.inkscape.org`).

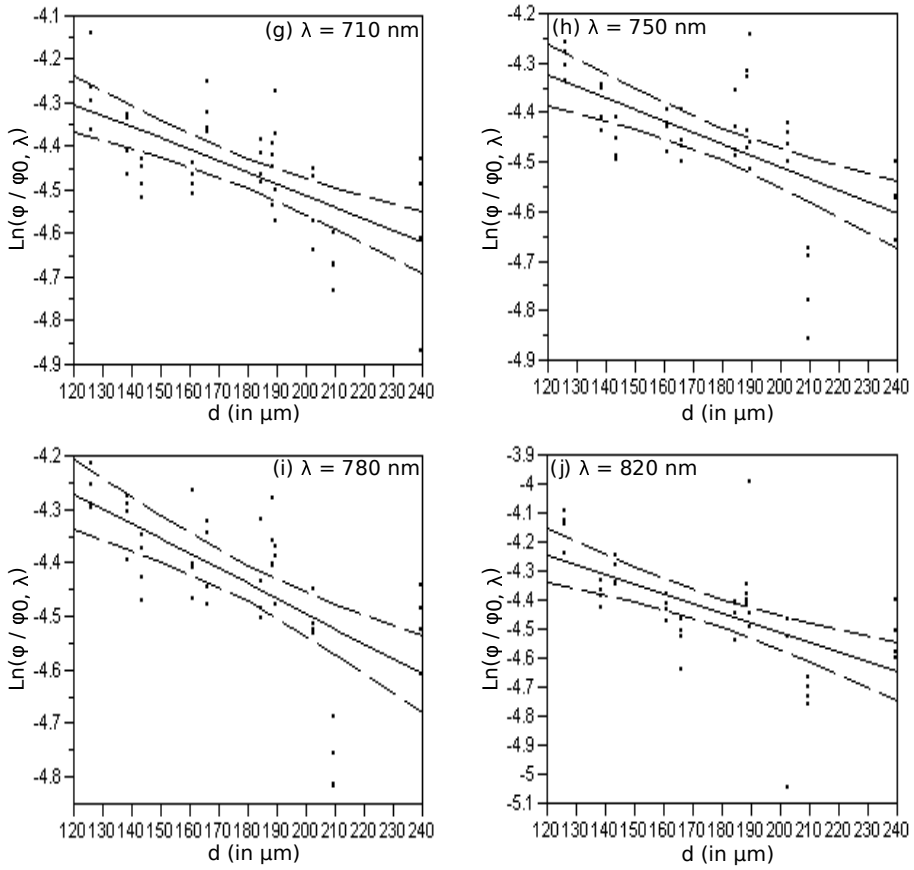

Figure 3.3: **Scatter plots and superimposed univariate regression model of data subsets of the main experimental study with varying cortical thickness and constant signal wavelength.** The natural logarithm of the normalised, attenuated light signal ($\ln(\Phi/\Phi_{0,\lambda})$) is plotted against the cortical thickness (d) at the following signal wavelengths (λ): (g) $710\,nm$; (h) $750\,nm$; (i) $780\,nm$; (j) $820\,nm$. The corresponding linear univariate regression model is superimposed on each scatter plot together with confidence curves to the 5%-significance level (graphs produced with JMP 5.0.1, modified with Inkscape 0.91, opensource vector graphics editor, `http://www.inkscape.org`).

Table 3.3: **Summary of linear univariate regression analyses of data subsets of the main experimental study** with varying cortical thickness (d) and constant signal wavelength (λ), μ_d corresponds to the attenuation coefficient of each subset.

λ in nm	Coefficient of Determination (R^2)	Estimate of μ_d (in mm^{-1})	Standard Error of the Estimate (in mm^{-1})	p-value
470	0.05	1.76	1.15	0.1351
505	0.15	2.55	0.93	0.0090
570	0.35	3.09	0.65	< 0.0001
590	0.35	4.32	0.91	< 0.0001
650	0.26	3.01	0.78	0.0004
680	0.25	2.84	0.75	0.0005
710	0.40	2.64	0.50	< 0.0001
750	0.37	2.35	0.48	< 0.0001
780	0.43	2.81	0.50	< 0.0001
820	0.35	3.36	0.71	< 0.0001

findings already imply that the influence of the signal wavelength on the attenuation of the light signal cannot be resolved with the experimental set up of this project. Further analyses of this result were performed with the multivariate regression model.

3.3.2 Multivariate Regression Analyses

The results of the non-linear regression model presented in equation 2.8 which was applied to the entire data set of the main experimental as well as to the modified set up study are summarized in table 3.5. A statistically significant exponential decrease of the light signal with increasing sample thickness could be shown in both studies as the 95 %-confidence intervals (CI_{95}) of the corresponding reduced scattering coefficient's scaling factors (a) were both located within the set of positive real numbers not including the zero (confidence interval of a within the main experimental study: $1.79\,mm^{-1} \leq CI_{95} \leq 3.60\,mm^{-1}$, confidence interval of a within the modified set up study: $2.11\,mm^{-1} \leq CI_{95} \leq 9.81\,mm^{-1}$). But a wavelength-dependence of the reduced scattering coefficient could not be found as the scattering power (b) introduced in equation 2.6 could not be shown to have a statistically significant influence on the regression model (confidence interval of b within the main experimental study: $-1.36 \leq CI_{95} \leq 0.81$, confidence interval of b within the the modified set up study: $-2.03 \leq CI_{95} \leq 2.05$). These two findings are in line with the univariate regression analyses presented in chapter 3.3.1.

Exclusion of variables showing no statistically significant effect within the main experimental study led to a linear regression model using only two of the initial four variables, a and K_0:

$$\ln\left(\frac{\Phi(d)}{\Phi_{0,\lambda}}\right) = \ln(K_0) - a\,d. \tag{3.1}$$

This model is superimposed on the entire data set of the main experimental study in figure 3.6 (a). The reduced scattering coefficient is equal to the variable a in this case ($\mu_s' = a =$

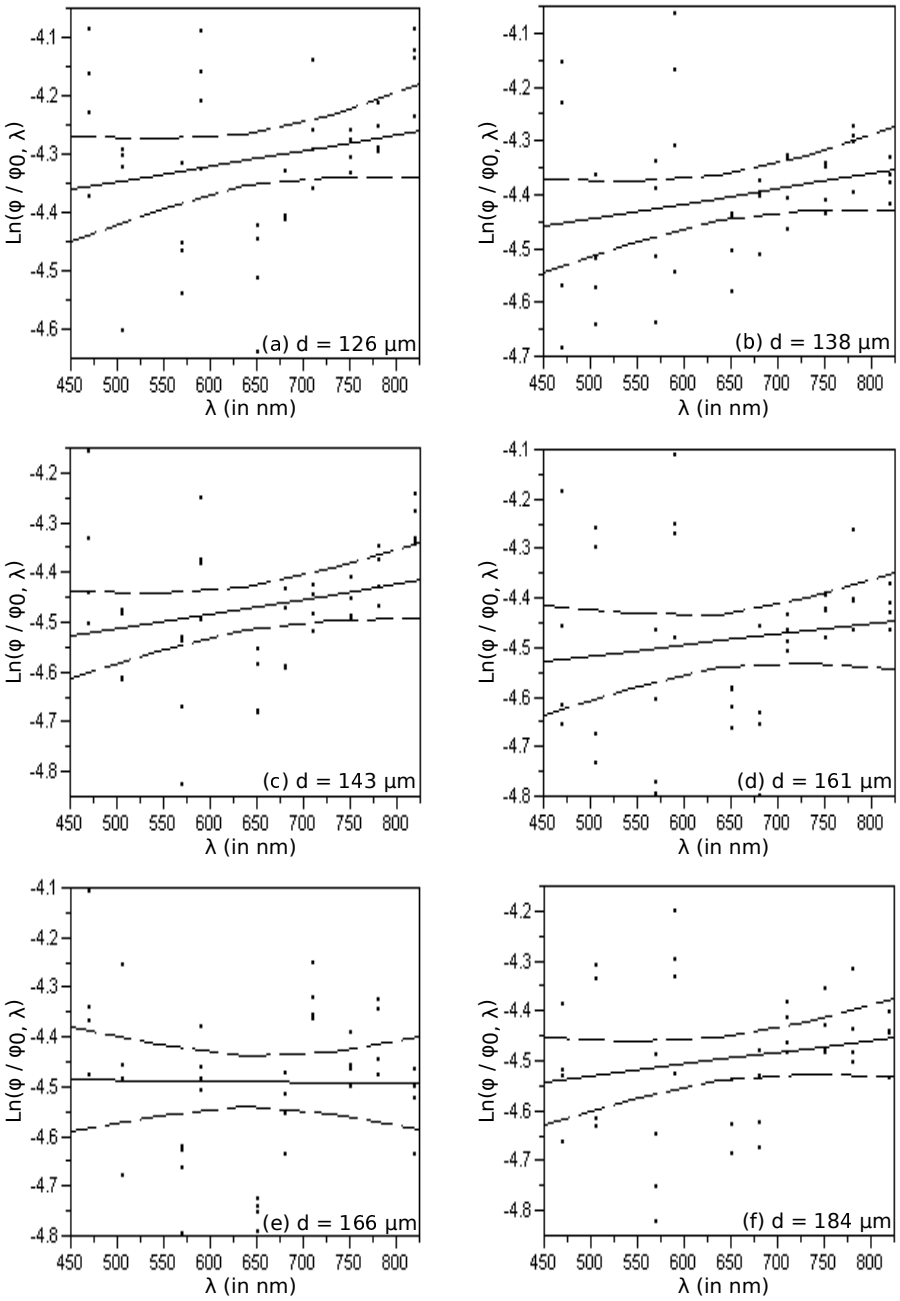

Figure 3.4: **Scatter plots and superimposed univariate regression model of data subsets of the main experimental study with varying signal wavelength and constant cortical thickness.** The natural logarithm of the normalised, attenuated light signal ($\ln(\Phi/\Phi_{0,\lambda})$) is plotted against the signal wavelength (λ) using the following bone samples with cortical thickness d: (a) sample 01 ($d = 126\,\mu m$); (b) sample 02 ($d = 138\,\mu m$); (c) sample 03 ($d = 143\,\mu m$); (d) sample 04 ($d = 161\,\mu m$); (e) sample 05 ($d = 166\,\mu m$); (f) sample 06 ($d = 184\,\mu m$). The corresponding linear univariate regression model is superimposed on each scatter plot together with confidence curves to the 5%-significance level (graphs produced with JMP 5.0.1, modified with Inkscape 0.91, opensource vector graphics editor, `http://www.inkscape.org`).

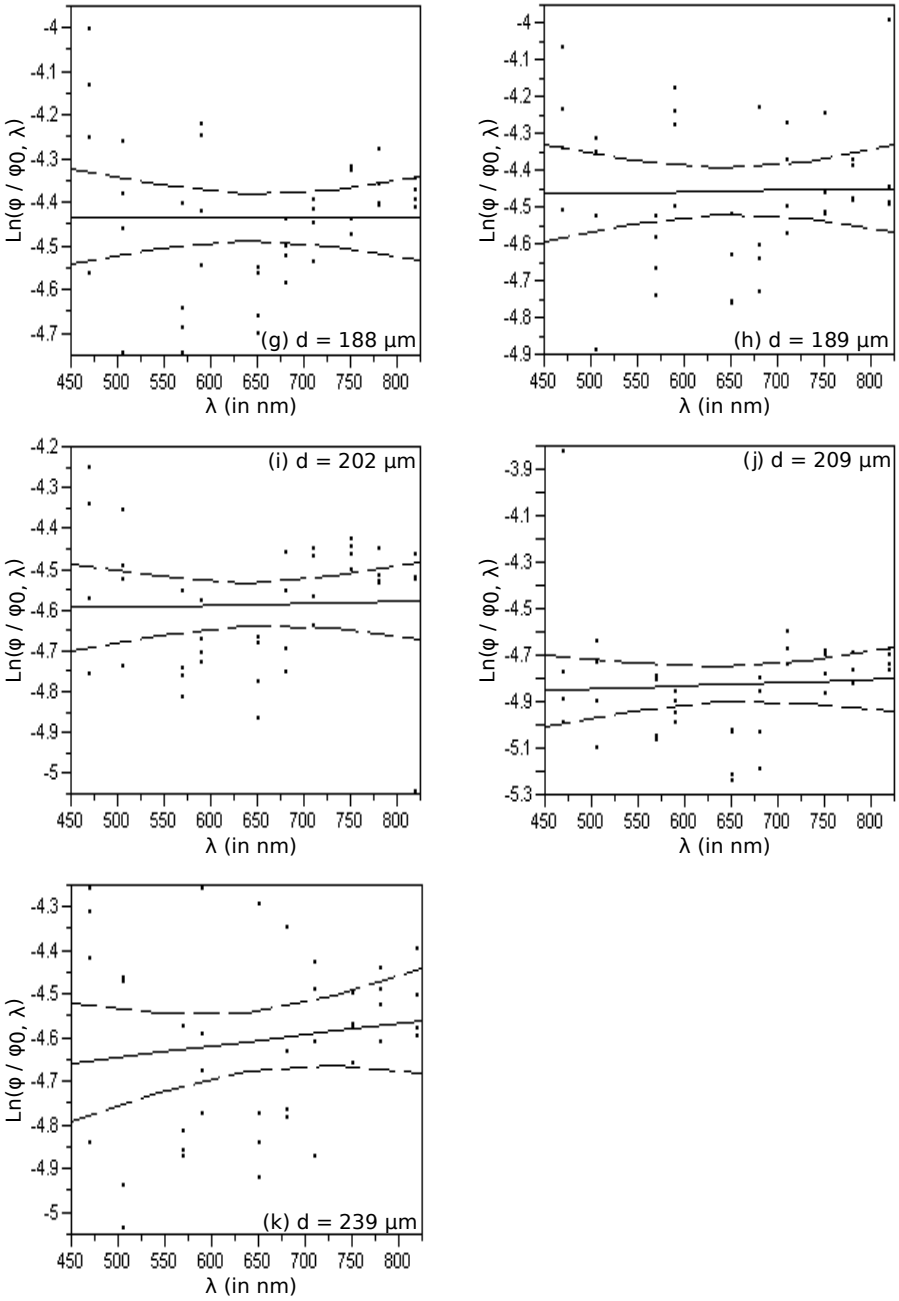

Figure 3.5: **Scatter plots and superimposed univariate regression model of data subsets of the main experimental study with varying signal wavelength and constant cortical thickness.** The natural logarithm of the normalised, attenuated light signal ($\ln(\Phi/\Phi_{0,\lambda})$) is plotted against the signal wavelength (λ) using the following bone samples with cortical thickness d: (g) sample 07 ($d = 188\,\mu m$); (h) sample 08 ($d = 189\,\mu m$); (i) sample 09 ($d = 202\,\mu m$); (j) sample 10 ($d = 209\,\mu m$); (k) sample 11 ($d = 239\,\mu m$). The corresponding linear univariate regression model is superimposed on each scatter plot together with confidence curves to the 5%-significance level (graphs produced with JMP 5.0.1, modified with Inkscape 0.91, opensource vector graphics editor, `http://www.inkscape.org`).

Table 3.4: **Summary of linear univariate regression analyses of data subsets of the main experimental study** with varying signal wavelength (λ) and constant cortical thickness (d), μ_λ corresponds to the attenuation coefficient of each subset.

Bone Sample	**Coefficient of Determination (R^2)**	**Estimate of μ_λ (in $10^{-4}\,nm^{-1}$)**	**Standard Error of the Estimate (in $10^{-4}\,nm^{-1}$)**	**p-value**
01	0.05	-2.66	1.93	0.1760
02	0.06	-2.84	1.86	0.1359
03	0.06	-2.93	1.87	0.1243
04	0.02	-2.17	2.37	0.3653
05	< 0.01	0.21	2.26	0.9251
06	0.04	-2.33	1.90	0.2271
07	< 0.01	0.11	2.34	0.9619
08	< 0.01	-0.39	2.82	0.8910
09	< 0.01	-0.42	2.29	0.8546
10	< 0.01	-1.31	3.34	0.6975
11	0.02	-2.62	2.89	0.3695

$2.87 \pm 0.28\,mm^{-1}$). The accuracy of the model was unchanged by this exclusion as the root mean square error was not substantially altered by this process. The wavelength-independent regression model including only a and K_0 as independent variables was also applied to the data of the modified set up study. The reduced scattering coefficient is equal to the variable a ($\mu'_{s\,mod} = a = 5.94 \pm 1.48\,mm^{-1}$) again, this model is superimposed on the entire data set of the modified set up study in figure 3.6 (b).

3.3.3 Comparison of the Reduced Scattering Coefficients

The absolute value of the reduced scattering coefficient of the main experimental study ($\mu'_s = 2.87 \pm 0.28\,mm^{-1}$) was found to be approximately two times smaller than its corresponding value of the modified set up study ($\mu'_{s\,mod} = 5.94 \pm 1.48\,mm^{-1}$).

The regression model presented in equation 2.9 was then applied to a combination of the entire data sets of both studies of this project. It was shown that the product $d\,\Omega$ has a statistically significant effect on this model (table 3.6). The operator therefore also has a statistically significant effect on the attenuation coefficient of this model (μ^*, cf. equation 2.11). The difference between the reduced scattering coefficients of the two multivariate regressions (μ'_s and $\mu'_{s\,mod}$) modelling each of the studies separately is therefore statistically significant.

Table 3.5: **Summary of multivariate regression analyses of the main experimental and modified set up study.** The behaviour of the natural logarithm of the normalised, attenuated light signal ($\ln(\Phi/\Phi_{0,\lambda})$) is modelled with respect to the sample thickness (d) and the wavelength (λ). Two regression models were calculated for each study: a complete model (equation 2.8) and another one including only the statistically significant (to the 5 %-level) estimates of the main experimental study (equation 3.1). a - scaling factor; b - scattering power; K_0 and ΔK - intercept and slope of the thickness-independent term ($K(\lambda)$) of the regression model; n - number of measurements included within each regression model; $Std.E.$ - standard error; $RMSE$ - root mean square error. The estimates high-lighted in boldface are statistically significant to the 5 %-level.

	Main Experimental Study		**Modified Set Up Study**	
Regression Model	**Equation 2.8**	**Equation 3.1**	**Equation 2.8**	**Equation 3.1**
$\boldsymbol{a}$ **(*Std.E.*) in** $\boldsymbol{mm^{-1}}$	**2.70 (0.46)**	**2.87 (0.28)**	**5.96 (1.97)**	**5.94 (1.48)**
$\boldsymbol{b}$ **(*Std.E.*)**	−0.27 (0.55)		0.01 (1.04)	
$\boldsymbol{K_0}$ **(*Std.E.*)**	**0.014 (0.005)**	**0.018 (0.001)**	9×10^{-5} (35×10^{-5})	$\mathbf{3 \times 10^{-4}}$ $\mathbf{(10^{-4})}$
$\boldsymbol{\Delta K}$ **(*Std.E.*)**	0.003 (0.004)		2×10^{-4} (3×10^{-4})	
RMSE	0.187	0.188	0.241	0.281
$\boldsymbol{n}$	440	440	42	42

Table 3.6: **Summary of multivariate regression analysis including the combined data of the main experimental and the modified set up study.** The behaviour of the natural logarithm of the normalised, attenuated light signal ($\ln(\Phi/\Phi_{0,\lambda})$) is modelled with respect to the sample thickness (d) and the operator (Ω). a - scaling factor; c_Ω - coefficient of Ω; $c_{d,\Omega}$ - coefficient of $d\,\Omega$; K_0 - constant corresponding to the thickness-independent term ($K(\lambda)$). Coefficient of determination: 0.98.

	Estimate	**Standard Error of the Estimate**	**p-value**
$\boldsymbol{c_\Omega}$	−4.54	0.03	0.0000
$\boldsymbol{c_{d,\Omega}}$ **in** $\boldsymbol{mm^{-1}}$	−3.07	1.08	0.0046
$\boldsymbol{a}$ **in** $\boldsymbol{mm^{-1}}$	3.14	0.28	< 0.0001
$\boldsymbol{\ln(K_0)}$	0.59	0.06	< 0.0001

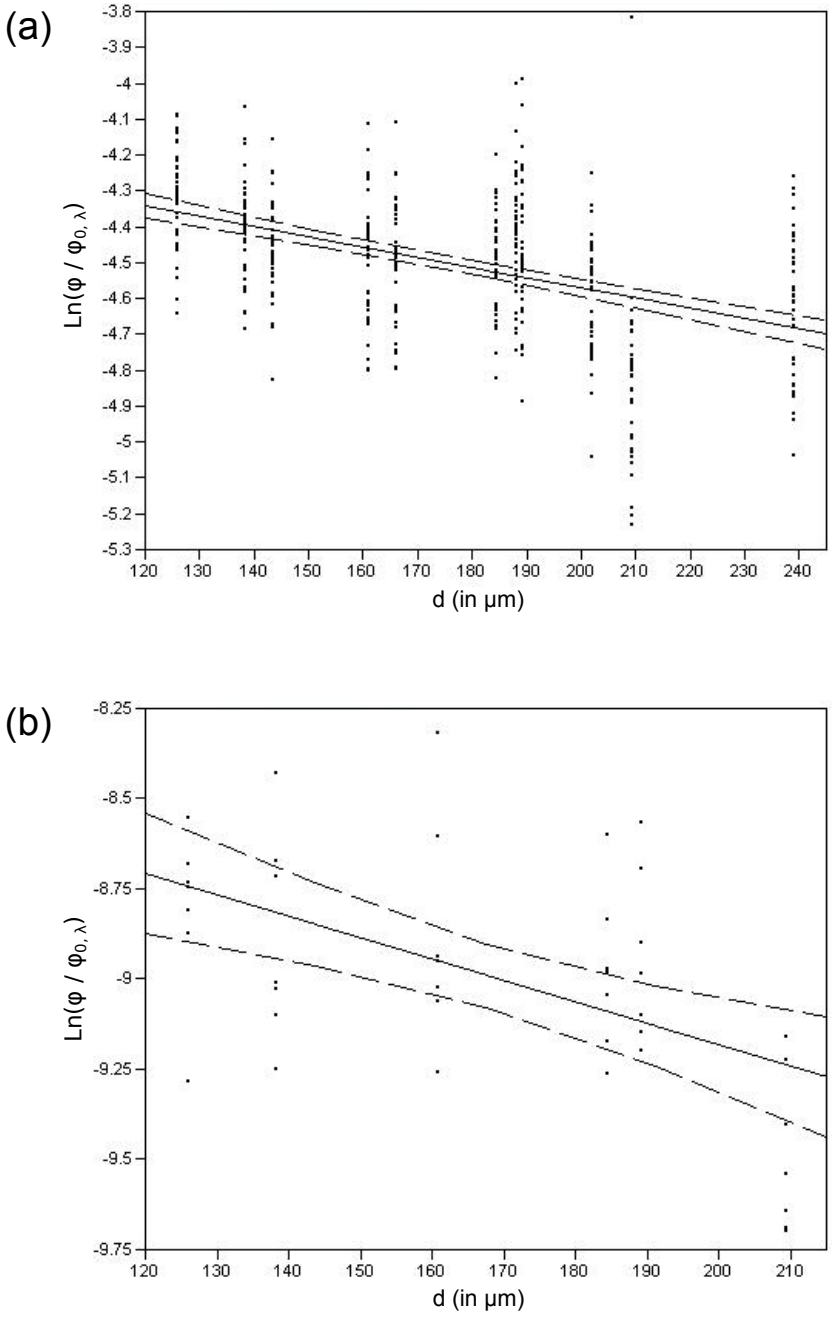

Figure 3.6: **Scatter plots and superimposed multivariate regression model of the main experimental (a) and the modified set up study (b).** The natural logarithm of the normalised, attenuated light signal ($\ln(\Phi/\Phi_{0,\lambda})$) is plotted against the cortical thickness (d) using the complete data set of the respective study measured with the entire wavelength spectrum of the project ($470\,nm \leq \lambda \leq 820\,nm$). The corresponding regression model only includes the statistically significant coefficients and is superimposed on each scatter plot together with confidence curves to the 5%-significance level. The slope of this regression model is equal to the coefficient a, which is in turn equal to the reduced scattering coefficient in this case: (a) $\mu'_s = a = 2.87 \pm 0.28\,mm^{-1}$; ($b$) $\mu'_{s\,mod} = a = 5.94 \pm 1.48\,mm^{-1}$ (graphs produced with JMP 5.0.1, modified with Inkscape 0.91, opensource vector graphics editor, `http://www.inkscape.org`).

CHAPTER 4

Discussion

4.1 The Attenuation Coefficient

4.1.1 Dependence on Cortical Thickness

The project showed that it is possible to resolve changes in the attenuated light signal (Φ) due to differences in the sample thickness (d). This was already implied by the univariate regression analyses of the data subsets and later confirmed in multivariate regression analyses showing a statistically significant influence of the attenuation coefficient (μ) within the main experimental and modified set up studies (cf. tables 3.3 and 3.5). The difference in the reduced scattering coefficients of the two studies (μ'_s and $\mu'_{s\,mod}$) shows the susceptibility of the attenuation measurements to changes in the experimental set up. Apart from minor changes, such as the operator, the inevitable change of the CCD-camera in between the two studies is regarded as the principal reason for the difference in the measured optical properties of bone tissue. This change resulted in an increased distance between the measuring bench and the CCD-camera itself. The other specifications of the camera stayed the same (e.g. focal length, aperture and sensor size). The maximum angle at which photons could be scattered away from their incoming straight path and still be detected by the camera was now smaller. A certain number of photons, which would have been detected within the main experimental study, were therefore lost within the modified set up study increasing the attenuation of the light signal and thus the reduced scattering coefficient as well. In summary, the effective area in which photons could be detected by the camera was reduced in accordance with the *inverse square law* (Bushberg *et al.*, 2012). This behaviour is visualized in figure 4.1. A further difference between the two studies is the number of measurements taken (n). In comparison to the modified set up study, approximately ten times more measurements were taken within the main experimental study. While the larger sample size explains the smaller standard error of the estimates, it does not explain the statistically significant difference of the reduced scattering coefficients of the two studies.

Differences can also be found when comparing the optical properties of the current project

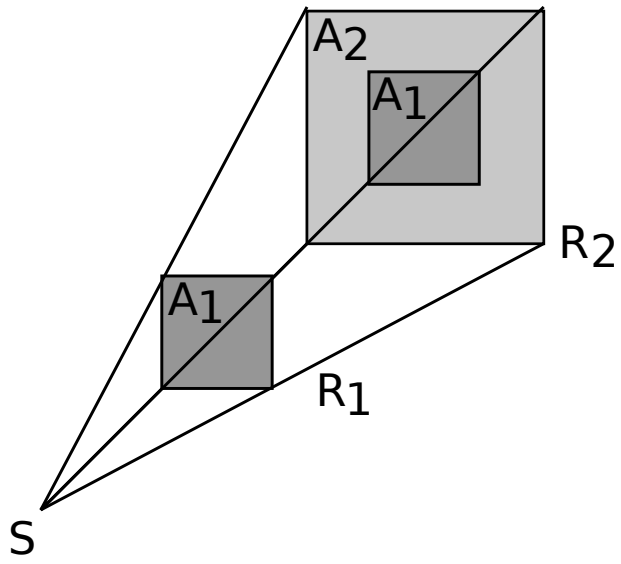

Figure 4.1: **Decrease of the effective area of photon detection within the modified set up study.** In order to detect the same number of photons after increasing the distance from the source S to the detector A from R_1 to R_2 (assuming a constant light signal at the source) requires an increase of the area by a factor of $(R_2/R_1)^2$: $A_2 = (R_2/R_1)^2\, A_1$ (*inverse square law*, Bushberg *et al.* (2012)). The effective area of photon detection is therefore reduced within the modified set up study as the sensor size remains unchanged, while the distance from the source to the detector is increased (graphics program: Inkscape 0.91, opensource vector graphics editor, `http://www.inkscape.org`).

to values presented in the literature. Firbank *et al.* (1993) ($\mu_s' = 2.63 \pm 0.44\, mm^{-1}$ at $650\, nm$) and Soleimanzad *et al.* (2017) ($\mu_s' = 2.29 \pm 0.12\, mm^{-1}$ at $705\, nm$) found reduced scattering coefficients of porcine and murine skull, respectively. These are very similar to the results of the main experimental study. On the other hand, Pitzschke *et al.* (2015) ($\mu_s' = 1.27 \pm 0.13$ (2 *standard deviations*) mm^{-1} at $671\, nm$) and Bevilacqua *et al.* (1999) ($\mu_s' = 0.9 \pm 0.1\, mm^{-1}$ at $674\, nm$) determined reduced scattering coefficients of human skull. These are smaller than the results of the main experimental study by a factor of two and three, respectively. The above described differences in μ_s' are further consequences of significant differences not only in the theoretical modelling but also in the experimental set up including the usage of tissue of different species and age as well as different processing and storing methods. This has already been discussed in reviews on modelling approaches and experimental data of optical properties of tissue by Cheong *et al.* (1990) and Jacques (2013). The former review stresses the importance of "both theoretical and experimental techniques" for the "reliability of optical properties" (Cheong *et al.*, 1990).

A very common technique in determining optical properties of biological tissue is the measurement of the diffuse transmittance through and reflectance from tissue samples within integrating spheres (e.g. Firbank *et al.* (1993) and Ugryumova *et al.* (2004), cf. chapter 1.2). This is a highly specialized technique to measure optical properties *ex vivo*. It ensures that photons which have sampled the tissue are not lost from detection. This is a main difference to the current experimental set up, where photons having sampled the tissue can get lost between measuring bench and CCD-camera. But as an FRI-device was deliberately chosen in order to determine optical properties of tissue to be later used to correct the light signal attenuation

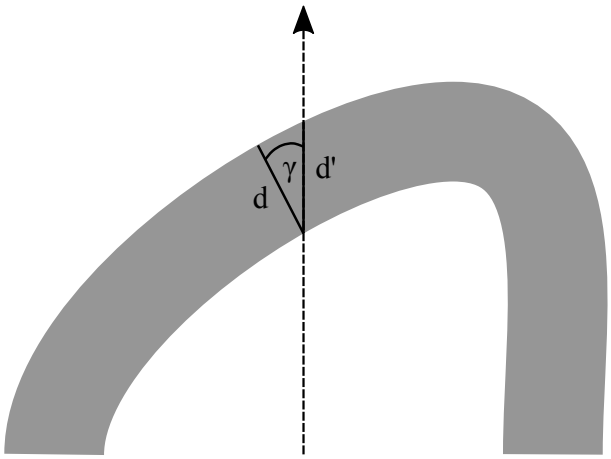

Figure 4.2: **Bone cortical thickness (d) versus photon path length (d′).** The photon path length inside the bone tissue is not identical to the cortical thickness for bone samples showing a skewed semi-circle cross section: $d = d' \cos(\gamma)$. The arrow represents the orientation of the light beam (graphics program: Inkscape 0.91, opensource vector graphics editor, `http://www.inkscape.org`).

within bio-molecular experiments, the partial loss of light signal needs to be accepted as one component of the attenuation within FRI-devices.

The geometry of the bone samples is a further specific difference of the current experimental set up compared to previous projects. The majority of the samples used within this project were not flat but rather had semi-circle cross sections (figure 2.2(a)) due to the preparation process described in chapter 2.1 and the desire to keep the geometry as close to later *in vivo*-applications as possible. The fact that the ideal semi-circle cross section was often skewed caused an effective increase in the cortical thickness (figure 4.2). This led to an underestimation of the photon path length inside the bone tissue and ultimately to an overestimated and therefore larger attenuation coefficient within the regression analyses. Additionally, differences in the scattering coefficient of up to 40 % were already found due to directional anisotropy of hydroxyapatite crystals and collagen in bone samples (Ugryumova *et al.*, 2004). Therefore the different geometries of the samples in this project also resulted in different orientations of the hydroxyapatite crystals and the collagen of the bone samples to the general direction of the light beam, which led to a further alteration of the attenuation coefficient.

4.1.2 Dependence on Signal Wavelength

Even though the reduced scattering coefficient was found to be of the same order of magnitude as in previous projects, the variable b governing its wavelength-dependence could not be shown to have a statistically significant effect on the multivariate regression analyses of the current project (table 3.5). This behaviour was already implied by the univariate regression analyses of the data subsets (table 3.4). A decrease of the reduced scattering coefficient with increasing signal wavelength was found in previous projects. Though this decrease was usually small (Wilson & Jacques, 1990) and the uncertainties large (e.g. Firbank *et al.* (1993), Ugryumova *et al.* (2004), Pitzschke *et al.* (2015), Bevilacqua *et al.* (1999), Soleimanzad *et al.* (2017)). Potential influences preventing a stronger dependence were considered for example the sample prepara-

tion and autofluorescence (Bevilacqua *et al.* (1999), Soleimanzad *et al.* (2017)). Within the current project, the wavelength-dependence could most likely not be resolved due to the specific experimental set up. As it is primarily designed for bio-molecular imaging and not attenuation measurements, it results in larger uncertainties due to the limitations already discussed above. These uncertainties disguise the small variations due to a wavelength-dependence of the reduced scattering coefficient. A statistically significant difference between reduced scattering coefficients at different wavelengths might be achieved using a larger wavelength spectrum. But this would not be practical due to the lack of corresponding fluorescent dyes to be used in later bio-molecular imaging.

The most pronounced relative changes in attenuation with wavelength were found in the literature within the absorption spectrum (Wilson & Jacques, 1990). This is due to the influence of blood and its major light signal attenuating component haemoglobin. Soleimanzad *et al.* (2017) showed a drastic drop of the absorption coefficient in murine skull with increasing signal wavelength ($\mu_a = 1.67 \pm 0.28\,mm^{-1}$ at $455\,nm$ and $\mu_a = 0.47 \pm 0.07 mm^{-1}$ at $705\,nm$). Important for the detection of this drop in absorption was the presence of blood within the bone sample. This was ensured by Soleimanzad *et al.* (2017) by taking measurements within one hour after dissection. Additionally, previous studies in which haemoglobin has been removed during the preparation process of the bone samples (either actively through chemicals or passively through storage in PBS) have shown that the absorption coefficient is up to two orders of magnitude smaller than the reduced scattering coefficient (e.g. Firbank *et al.* (1993), Ugryumova *et al.* (2004), Bevilacqua *et al.* (1999), Soleimanzad *et al.* (2017)). Within the current project scattering and absorption could not be differentiated (cf. chapter 2.4). As haemoglobin was removed from the bone tissue samples during the preparation and storage in PBS, it can be assumed that the absorption is up to two orders of magnitude smaller than the scattering within the current project as well. The standard errors of the scattering coefficients of both studies are at least one tenth of their estimates. The absorption coefficient can therefore be considered to be smaller than the reduced scattering coefficient's uncertainty. The wavelength-dependence of the absorption is therefore hidden by the reduced scattering.

As wavelength-dependent changes of the attenuated light signal could not be resolved, a correction for attenuation processes in molecular imaging applying a wavelength spectrum of commonly used fluorescent dyes is not possible with the current set up using standard FRI-equipment alone (cf. chapter 1.3.1). So unless an improvement of the presented set up leads to the resolution of the wavelength-dependence of the attenuation, applying different fluorescent dyes to correct for attenuation by using a uni-modal optical approach like ratiometry is not possible. Other correction techniques can nevertheless be used with the current results, an additional imaging method is needed though to determine the tissue thickness, this can be done with μCT (cf. chapter 1.3.2.2).

4.2 Thickness Independent Attenuation

Similar to the behaviour of the reduced scattering coefficient discussed in the previous chapter, it was neither possible to resolve a wavelength-dependence of the term K, which was introduced to account for bone thickness-independent attenuation effects. Even though the majority of

the attenuation due to this term was expected to be caused by the refraction at interfaces, the influence of other factors, such as the surface roughness, could not be anticipated due to their random behaviour. An underlying wavelength-dependence was thus distorted by these random influences to K.

The wavelength-independent regression model including only the statistically significant variables a and K_0 (equation 3.1) showed that K_0 dominates the exponential term even for the thickest bone samples. An approximate reduction of 45 % of the initially unattenuated light signal was found to be due to scattering processes using the thickest bone sample included in both studies ($e^{-\mu_s' d} \approx 0.55$ for $\mu_s' = 2.87\, mm^{-1}$ and $d = 209\, \mu m$), while thickness-independent processes like specular reflection reduced this signal by approximately 98 % ($K_0 \approx 0.02$) within the main experimental study. This was found to be even more pronounced within the modified set up study yielding 71 % and 99.97 % reductions, respectively (cf. table 3.5). In analogy to the scattering coefficients found in the two studies of the current project, the difference in K_0 can be explained by the the increased spatial separation again, which led to a smaller effective area of detection of the CCD-camera. Thus, a certain number of photons being deviated from their incoming straight path by these surface effects, that would have been detected within the main experimental study, were lost within the modified set up study.

A potential improvement is offered by refractive index matching (e.g. applied by Ugryumova *et al.* (2004)). It is a method which reduces the reflection at interfaces by immersing the tissue samples in a saline solution when executing attenuation measurements. The difference in refractive indices of the two bordering media is thus reduced minimising the deviation of photons due to refraction. It is assumed that this will not only decrease the light signal attenuation due to K in comparison with absorption and scattering, but it will also reduce the susceptibility of changes made to the experimental set up as a larger number of photons should be detected even with a smaller effective sensor size due to a smaller angular distribution of photons. This method ultimately leads to a set up closer to *in vivo*-measurements as the bone surface borders with a medium having a closer physical resemblance to soft tissue.

4.3 Tissue Mineral Density and Attenuation

Even though variations in ρ_{TMD} led to resolvable changes in light attenuation in previous studies, including Ugryumova *et al.* (2004), this variable was excluded from the regression analyses of the current project. This was not due to a general lack of resolving variations in attenuation due to changes in ρ_{TMD} with FRI-devices. But as d was the only bone sample property which was controlled within this project and all samples were chosen from mice with a physiological bone structure and mineralisation, the variability of ρ_{TMD} turned out to be very small. This variable was therefore considered constant and its variations due to natural, random differences between the samples. To determine the influence of ρ_{TMD} on the light signal attenuation in FRI further studies are needed using bone samples with a large range of ρ_{TMD}.

4.4 Conclusion

It was shown with this project that optical properties of cortical bone tissue leading to the attenuation of light signals can be resolved using an FRI-device commonly used for bio-molecular research. This allows to quantify the attenuation of light signals by bone tissue. But the correction of attenuated light signals is limited with this set up. It thus requires the use of another imaging modality, such as μCT. Ratiometric approaches might be applicable in the future, if the current experimental set up is improved allowing the resolution of the wavelength-dependence of the attenuation.

It was also shown that the specific set up influences the measured optical properties of bone tissue. Standard values of these properties thus need to be handled with care. And it is highly recommended to use optical properties determined with a similar experimental set up to gain the most accurate results when correcting attenuated light signals in bio-molecular research.

CHAPTER 5

Summary

Fluorescence reflectance imaging is a powerful technique to study microscopic processes on a microscopic scale in bio-molecular research. This enables for example *in vivo*-monitoring of metabolic and oncologic processes in bone tissue of small animals. However, the detection of light signals originating from biological structures labelled with fluorescent dyes is subject to attenuation processes occuring in the surrounding tissue. This introduces an unwanted bias, which has already been quantified in many previous studies in order to correct the measured light signal for attenuation. It was thus found that the attenuation does not only depend on the tissue type under examination but on the specific set up of the experiment as well.

It was therefore the aim of this project to quantify light signal attenuation in bone tissue as a function of cortical thickness (d) and signal wavelength (λ) to assess the feasibility to correct for attenuation effects in molecular imaging of small animals employing a commonly used experimental set up including fluorescence reflectance imaging.

Bone samples were prepared from diaphyses of murine femora and tibiae. Micro-computed tomography was then used to determine the cortical thickness and the tissue mineral density of these samples, which were then used to attenuate well defined light signals produced by light emitting diodes. These were chosen to match the absorption and emission spectra of commonly used fluorescent dyes ($470\,nm \leq \lambda \leq 820\,nm$). Fluorescence reflectance imaging was used to measure the attenuated signals.

An exponential decay of the light signal with increasing cortical thickness (for $126\,\mu m \leq d \leq 239\,\mu m$) was observed. The attenuation was quantified with the reduced scattering coefficient ($\mu_s' = 2.87 \pm 0.28\,mm^{-1}$). This parameter was derived from a multivariate regression model that was based on the diffusion approximation to the transport theory. But it was not possible to resolve the wavelength-dependence of the reduced scattering coefficient within the chosen wavelength spectrum. A second study with a modified set up yielded qualitatively similar data with a reduced scattering coefficient which showed a significant difference compared to the corresponding coefficient of the main experimental study: $\mu_{s\,mod}' = 5.94 \pm 1.48\,mm^{-1}$. It was thus also confirmed with the current project that the acquired data is substantially affected by

the specifics of the experimental set up.

The results of this project show that a correction for attenuation effects using optical data from fluorescence reflectance imaging is feasible when combined with another imaging modality, such as micro-computed tomography. Using only fluorescence reflectance imaging in a uni-modal approach, such as ratiometry, to correct attenuated light signals is not feasible with the current experimental set up due to the limited wavelength-dependence of the derived optical bone tissue properties. This project also clarified the importance of the specific experimental set up. It is therefore strongly suggested to perform calibration measurements prior to future bio-molecular studies trying to correct for tissue attenuation in order to obtain quantitative results from fluorescent reflectance imaging, such as the fluorescent dye concentration. Both experimental set ups should be as similar to each other as possible to obtain reliable data.

Bibliography

Abramowitz, M, & Davidson, MW. 2019 (Accessed July 2019). *Olympus®: Microscopy Resource Center: Introduction to fluorescence.* `https://www.olympus-lifescience.com/de/microscope-resource/primer/lightandcolor/fluorointroduction/`.

Abramowitz, M, Herman, B, Murphy, DB, & Davidson, MW. 2019 (Accessed July 2019). *Olympus®: Microscopy Resource Center: Anatomy of the fluorescence microscope.* `https://www.olympus-lifescience.com/de/microscope-resource/primer/techniques/fluorescence/anatomy/fluoromicroanatomy/`.

Baird, E, & Taylor, G. 2017. X-ray micro computed-tomography. *Curr. Biol.*, **27**, R289–R291. doi: 10.1016/j.cub.2017.1.066.

Bevilacqua, F, Piguet, D, Marquet, P, Gross, JD, Tromberg, BJ, & Depeursinge, C. 1999. In vivo local determination of tissue optical properties: applications to human brain. *Appl. Opt.*, **38**(22), 4939–4950. doi: 10.1364/AO.38.004939.

Boerckel, JD, Mason, DE, McDermott, AM, & Alsberg, E. 2014. Microcomputed tomography: approaches and applications in bioengineering. *Stem Cell Research & Therapy*, **5**(6), 144. doi: 10.1186/scrt534.

Bouxsein, ML, Boyd, SK, Christiansen, BA, Guldberg, RE, Jepsen, KJ, & Müller, R. 2010. Guidelines for assessment of bone microstructure in rodents using micro-computed tomography. *JBMR*, **25**(7), 1468–1486. doi: 10.1002/jbmr.141.

Bradley, RS, & Thorniley, MS. 2006. A review of attenuation correction techniques for tissue fluorescence. *Journal of the royal society Interface*, **3**(6), 1–13. doi: 10.1098/rsif.2005.0066.

Bruhn, HD, Junker, R, Schäfer, H, & Schreiber, S. 2011. *LaborMedizin: Indikationen, Methodik und Laborwerte. Pathophysiologie und Klinik. 3. Auflage.* Schattauer, Stuttgart.

Bushberg, JT, Seibert, JA, Leidholdt, EM, & Boone, JM. 2012. *The essential physics of medical imaging, third edition.* Lippincott Williams & Wilkins, Philadelphia.

Chalfie, M, Tu, Y, Euskirchen, G, Ward, WW, & Prasher, DC. 1994. Green fluorescent protein as a marker for gene expression. *Science*, **263**(5148), 802–805. doi: 10.1126/science.8303295.

Cheong, WF, Prahl, SA, & Welch, AJ. 1990. A review of the optical properties of biological tissues. *IEEE Journal of Quantum Electronics*, **26**(12), 2166–2185. doi: 10.1109/3.64354.

Cox, G. 2019. *Fundamentals of fluorescence imaging.* Jenny Stanford Publishing, Singapore.

Desmettre, T, Devoisselle, JM, & Mordon, S. 2000. Fluorescence properties and metabolic features of indocyanine green (ICG) as related to angiography. *Survey of ophthalmology*, **45**(1), 15–27. doi: 10.1016/S0039-6257(00)00123-5.

du Plessis, A, Broeckhoven, C, Guelpa, A, & le Roux, SG. 2017. Laboratory x-ray micro-computed tomography: a user guideline for biological samples. *GigaScience*, **6**, 1–11. doi: 10.1093/gigascience/gix027.

Filonov, GS, Piatkevich, KD, Ting, LM, Zhang, J, Kim, K, & Verkhusha, VV. 2011. Bright and stable near-infrared fluorescent protein for in vivo imaging. *Nature biotechnology*, **29**(8), 757–761. doi: 10.1038/nbt.1918.

Firbank, M, Hiraoka, M, Essenpreis, M, & Delpy, DT. 1993. Measurement of the optical properties of the skull in the wavelength range 650-950 nm. *Physics in medicine and biology*, **38**(4), 503–510. doi: 10.1088/0031-9155/38/4/002.

Graves, EE, Weissleder, R, & Ntziachristos, V. 2004. Fluorescence molecular imaging of small animal tumor models. *Curr. Mol. Med.*, **4**(4), 419–430. doi: 10.2174/1566524043360555.

Grehn, F. 2008. *Augenheilkunde, 30. Auflage.* Springer Medizin Verlag, Heidelberg.

Jacques, SL. 2013. Optical properties of biological tissue: a review. *Phys. Med. Biol.*, **58**(11), R37–R61. doi: 10.1088/0031-9155/58/11/R37.

Kauffmann, G, Sauer, R, & Weber, W. 2011. *Radiologie: Bildgebende Verfahren, Strahlentherapie, Nuklearmedizin und Strahlenschutz. 4. Auflage.* Elsevier GmbH, Urban & Fischer Verlag, München.

Kersten, RT. 1983. *Einführung in die optische Nachrichtentechnik. Physikalische Grundlagen, Einzelelemente und Systeme.* Springer Verlag, Berlin.

NobelPrize.org, Nobel Media AB 2019. 2019 (Accessed July 2019). *The Nobel Prize in chemistry 2008.* `https://www.nobelprize.org/prizes/chemistry/2008/summary/`.

Ntziachristos, V, Ripoll, J, Wang, LV, & Weissleder, R. 2005. Looking and listening to light: the evolution of whole-body photonic imaging. *Nature biotechnology*, **23**(3), 313–320. doi: 10.1038/nbt1074.

PerkinElmer, Inc. 2010a (Accessed November 2016). *Technical data sheet. Fluorescent imaging agent. Osteosense® 750EX.* `https://www.perkinelmer.com/lab-solutions/resources/docs/TDS_NEV10053EX%20OsteoSense%20750%20EX-TD.pdf`.

PerkinElmer, Inc. 2010b (Accessed November 2016). *Technical data sheet. Fluorescent imaging agent. Osteosense® 800.* https://www.perkinelmer.com/lab-solutions/resources/docs/TCH_NEV11105-OsteoSense800-TD.pdf.

Piston, DW, Patterson, GH, Lippincott-Schwartz, J, Claxton, NS, & Davidson, MW. 2019a (Accessed July 2019). *Nikon®: MicroscopyU: Introduction to fluorescent proteins.* https://www.microscopyu.com/techniques/fluorescence/introduction-to-fluorescent-proteins.

Piston, DW, Campbell, RE, Day, RN, & Davidson, MW. 2019b (Accessed July 2019). *Zeiss®: Carl Zeiss Microscopy Online Campus: Introduction to fluorescent proteins.* http://zeiss-campus.magnet.fsu.edu/articles/probes/fpintroduction.html.

Pitzschke, A, Lovisa, B, Seydoux, O, Zellweger, M, Pfleiderer, M, Tardy, Y, & Wagnières, G. 2015. Red and NIR light dosimetry in the human deep brain. *Phys. Med. Biol.*, **60**(7), 2921–2937. doi: 10.1088/0031-9155/60/7/2921.

Plattner, H, & Hentschel, J. 2006. *Zellbiologie. 3. Auflage.* Georg Thieme Verlag, Stuttgart.

Polom, K, Murawa, D, Rho, YS, Nowaczyk, P, Hünerbein, M, & Murawa, P. 2011. Current trends and emerging future of indocyanine green usage in surgery and oncology. *Cancer*, **117**(21), 4812–4822. doi: 10.1002/cncr.26087.

Prasher, DC, Eckenrode, VK, Ward, WW, Prendergast, FG, & Cormier, MJ. 1991. Primary structure of the Aequorea victoria green-fluorescent protein. *Gene*, **111**(2), 229–233. doi: 10.1016/0378-1119(92)90691-H.

Prokop, M, Galanski, M, van der Molen, AJ (Co-Editor), Schaefer-Prokop, CM (Co-Editor), Engelke, C (Contributor), Jörgensen, M (Contributor), Lehmann, KJ (Contributor), Leppert, A (Contributor), & von Smekal, U (Contributor). 2003. *Spiral and multislice computed tomography of the body.* Thieme, Stuttgart.

Roithner Lasertechnik GmbH. 2020 (Accessed November 2020). *Technical data sheets. Light emitting diodes. Standard devices.* http://www.roithner-laser.com/led_diverse.html.

Sanderson, MJ, Smith, I, Parker, I, & Bootman, MD. 2014. Fluorescence microscopy. *Cold Spring Harb. Protoc.*, **10**, 1042–1065. doi: 10.1101/pdb.top071795.

Schmitt, JM, Zhou, GX, Walker, EC, & Wall, RT. 1990. Multilayer model of photon diffusion in skin. *JOSA A*, **7**(11), 2141–2153. doi: 10.1364/JOSAA.7.002141.

Shcherbo, D, Merzlyak, EM, Chepurnykh, TV, Fradkov, AF, Ermakova, GV, Solovieva, EA, Lukyanov, KA, Bogdanova, EA, Zaraisky, AG, Lukyanov, S, & Chudakov, DM. 2007. Bright far-red fluorescent protein for whole-body imaging. *Nature methods*, **4**(9), 741–746. doi: 10.1038/NMETH1083.

Shu, X, Royant, A, Lin, MZ, Aguilera, TA, Lev-Ram, V, Steinbach, PA, & Tsien, RY. 2009. Mammalian expression of infrared fluorescent proteins engineered from a bacterial phytochrome. *Science*, **324**(5928), 804–807. doi: 10.1126/science.1168683.

Soleimanzad, H, Gurden, H, & Pain, F. 2017. Optical properties of mice skull bone in the 455- to 705-nm range. *J. Biomed. Opt.*, **22**(1), 010503–1–010503–4. doi: 10.1117/1.JBO.22.1.010503.

Spring, KR, & Davidson, MW. 2019 (Accessed July 2019). *Nikon®: MicroscopyU: Introduction to fluorescence microscopy.* `https://www.microscopyu.com/techniques/fluorescence/introduction-to-fluorescence-microscopy`.

Ugryumova, N, Matcher, SJ, & Attenburrow, DP. 2004. Measurement of bone mineral density via light scattering. *Physics in medicine and biology*, **49**(3), 469–483. doi: 10.1088/0031-9155/49/3/009.

Vogel, H. 1999. *Gerthsen Physik, 20. Auflage.* Springer Verlag, Berlin.

Wilson, BC, & Jacques, SL. 1990. Optical reflectance and transmittance of tissues: principles and applications. *IEEE Journal of Quantum Electronics*, **26**(12), 2186–2199. doi: 10.1109/3.64355.

Zaheer, A, Lenkinski, RE, Mahmood, A, Jones, AG, Cantley, LC, & Frangioni, JV. 2001. In vivo near-infrared fluorescence imaging of osteoblastic activity. *Nat. Biotechnol.*, **19**, 1148–1154. doi: 10.1038/nbt1201-1148.

List of Figures

List of Tables

Acknowledgements

First and foremost, I would like to express my gratitude to Prof. Dr. rer. nat. Claus-Christian Glüer, head of the Section Biomedical Imaging within the Department of Radiology and Neuroradiology. I am grateful for being given the oportunity to apply my combined knowledge in the fields of physics and medicine to a stimulating topic. I am also grateful for his guidance always letting me see the big picture again whenever I was lost in too much detail.

Within the years that I have been working on this project, I was lucky to meet many excellent people, whom I am very grateful for their unconditional support. Special thanks need to be given to Dr. Graeme Campbell, who was my supervisor in the beginning of this project, and to Angelika Schmalzl, who was the second operator performing the modified set up study.

I am especially grateful for the support of my family and friends, who always soothed me in the emotional ups and downs that go along with such an endeavour.